Low-temperature water-gas shift on Pt/Ce$_{1-x}$La$_x$O$_{2-\delta}$: Effect of Ce/La ratio

Klito C. Petallidou, Angelos M. Efstathiou*

Department of Chemistry, Heterogeneous Catalysis Laboratory, University of Cyprus, University Campus, P.O. Box 20537, CY 1678 Nicosia, Cyprus

ARTICLE INFO

ABSTRACT

Pt nanoparticles (1.0–1.4 nm size) supported on Ce$_{1-x}$La$_x$O$_{2-\delta}$ (x = 0.0, 0.2, 05, 0.8 and 1.0) carriers, the latter prepared by the citrate sol–gel method, were tested toward the water-gas shift (WGS) reaction in the 200–400 °C range. A deep insight into the effect of Ce/La atom ratio of support chemical composition on the catalytic performance (CO conversion *vs.* temperature and stability) and kinetic rates of Pt-loaded catalysts was realized after employing HAADF/STEM, *in situ* Raman and DRIFT spectroscopies under different gas atmospheres, temperature-programmed surface reaction (TPSR) in He and O$_2$/He gas atmospheres following WGS reaction, CO-TPD, *in situ* UV–vis/DRS, oxygen storage capacity measurements, and transient ^{18}O-isotopic exchange studies followed by WGS reaction. It was found that doping of ceria with 20 at.% La^{3+} has increased significantly the catalytic activity of 0.5 wt% Pt/Ce$_{0.8}$La$_{0.2}$O$_{2-\delta}$ solid in the 250–350 °C range, whereas addition of 50–80 at.% La^{3+} in ceria caused a negative effect on the CO conversion with respect to pure ceria. It was found that the Ce/La atom ratio in Ce$_{1-x}$La$_x$O$_{2-\delta}$ influences the catalytic site reactivity (k) along the Pt-support interface. The optimum La^{3+}-dopant concentration of 20 at.% (Ce/La = 4/1) used in Pt/Ce$_{0.8}$La$_{0.2}$O$_2$ compared to the worst one of 80 at.% (Pt/Ce$_{0.2}$La$_{0.8}$O$_{2-\delta}$, Ce/La = 1/4) correlates with (i) the higher specific kinetic rate per length of Pt-support interface (μmol CO cm^{-1} s^{-1}), (ii) the higher concentration of oxygen vacant sites, (iii) the lower amount (μmol/g^{-1}) of "carbon" accumulated during WGS and best stability with time on stream, (iv) the lower apparent activation energy (kcal mol^{-1}) of WGS reaction, (v) the lower degree toward Pt oxidation (largest Pt^{2+}/Pt^{4+} ratio), (vi) the lower Ce$_{1-x}$La$_x$O$_{2-\delta}$ support energy band gap, and (vii) the lower mobility of surface lattice oxygen.

1. Introduction

The water-gas shift (WGS) reaction (Eq. (1)) first reported in 1888 is considered as a very important step in the industrial process of hydrogen production (*e.g.*, steam reforming of natural gas) used for the manufacturing of highly added value chemicals, such as ammonia and petroleum refinery products [1,2]. The interest in the low-temperature WGS reaction has grown significantly in the last two decades as a result of the rapid advancements made in H$_2$ fuel cell technologies for power production [3,4]. The important role of WGS as part of the reaction network of hydrocarbon reforming toward H$_2$ formation is to reduce the CO in the reformate gas to concentrations less than 10 ppm in order to avoid the deleterious effect of CO on fuel cell electrodes [5]. The WGS reaction (1) is reversible, moderately exothermic and equilibrium limited.

$$CO(g) + H_2O(g) \leftrightharpoons CO_2(g) + H_2(g), \quad \Delta H^o = -41 \text{ kJ/mol} \tag{1}$$
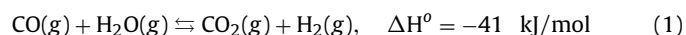
For many decades, Fe$_3$O$_4$/Cr$_2$O$_3$ catalysts are used in the high-temperature industrial WGS (350–450 °C), and CuO/ZnO/Al$_2$O$_3$ in the low-temperature WGS (180–250 °C). The latter LT-WGS catalysts are pyrophoric and require long-time period for activation, features that make them unsuitable for fuel cell applications [6]. Attempts are now focused toward the development of new and robust non pyrophoric low-loading supported noble metal catalysts which exhibit high stability and activity toward LT-WGS without any need for special activation procedures prior to use.

CeO$_2$-based metal oxides have been widely studied as supports of noble metals (*e.g.* Pt, Rh, Ru, Pd, Au) toward the WGS reaction [3,7–15]. Reducible metal oxide-supported Pt catalysts were found to exhibit higher activity compared to Rh, Ru or Pd [7]. Pt/Ce$_{0.8}$Zr$_{0.2}$O$_2$ was found to exhibit better catalytic performance compared to Pt/Ce$_{0.2}$Zr$_{0.8}$O$_2$ due to higher Pt dispersion, enhanced reducibility of support, and higher oxygen storage capacity (OSC), properties influenced by the chemical composition of Ce$_{0.8}$Zr$_{0.2}$O$_2$ support [10]. The addition of 50 at.% Ca^{2+} in ceria enhanced the WGS catalytic performance of Pt/Ca^{2+}–CeO$_2$ [12], and the WGS activity of Pt/Ce$_{0.5}$M$_{0.5}$O$_x$ (M = Ba, Hf, La, Y, Zn) was found to depend

on the nature of dopant used in the support chemical composition [13]. The addition of dopant in CeO_2 caused an enhancement in the reducibility of $Ce_{0.5}M_{0.5}O_x$ support and the rate of formate decomposition [13]; formate was suggested as an important reaction intermediate.

It was reported [16–19] that typical gas compositions $(CO/CO_2/H_2/H_2O/C_xH_y)$ of the outlet stream from a reformer cause progressive deactivation of supported metal catalysts. This could be attributed to the irreversible reduction of support [16], the formation of stable carbonates on the catalyst surface [6,17], and to the sintering of metal phase [18,19]. Addition of basic oxides to Pt/CeO_2 increased the activity and stability of the resulting catalyst, and favored decomposition of formate species, the latter suggested as an active reaction intermediate [6].

Two main mechanisms for the WGS reaction carried on reducible metal oxide-supported metal catalysts were proposed in the literature [2,14,20–24]: (i) the *regenerative or redox* mechanism and (ii) the *adsorptive or associative* mechanism. We have recently reported [23] that on the present $Pt/Ce_{1-x}La_xO_{2-\delta}$ catalysts the WGS reaction follows both the *redox and associative formate/carboxyl* mechanisms in the 250–300 °C range, where the extent of participation of each mechanism to the overall reaction rate is influenced by the support chemical composition. A reactive zone around each Pt nanoparticle is formed within which *active* OH/H and formate/carboxyl species reside, the concentration of which is largely influenced by the support chemical composition (Ce/La atom ratio). In fact, the extent of this reactive zone was on the average of the order of one lattice constant of support (3–4 Å), showing for the first time that practically the majority of active sites are present along the Pt-support interface.

In the present work we report on the catalytic behavior of $Ce_{1-x}La_xO_{2-\delta}$ ($x = 0$, 0.2, 0.5, 0.8 and 1.0) solids synthesized by the citrate sol–gel method and used as supports of 0.5 wt% Pt. A suite of techniques such as H_2-TPD, HAADF/STEM, CO-TPD, *in situ* UV–vis/DRS, *in situ* Raman, OSC, ^{18}O transient isotopic exchange followed by WGS reaction, and *in situ* DRIFTS-CO were used in an attempt to correlate several of the physicochemical properties of the solids with their catalytic activity. Temperature-programmed oxidation (TPO) was also performed to measure the amount of "carbon" accumulated on the catalyst surface under WGS reaction conditions, and relate this to the catalyst's activity behavior as a function of time on stream.

2. Experimental

2.1. Catalyst preparation

The preparation of $Ce_{1-x}La_xO_{2-\delta}$ ($x = 0.0$, 0.2, 0.5, 0.8 and 1.0) solid supports was carried out using the citrate sol–gel method. In particular, 3.7995 g of $Ce(NO_3)_3 \cdot 6H_2O$ and 3.7889 g of $La(NO_3)_3 \cdot 6H_2O$ (based on $Ce_{0.5}La_{0.5}O_{2-\delta}$ composition) were dissolved in distilled water to form a 0.175 M solution of total metal ions. The solution pH was kept at 2.0 by dropwise addition of nitric acid solution (5 M). Then, citric acid of 1.5 times the total molar amount of metal ions (M_{tot}) in solution was added. The resulting solution was subsequently heated to 70 °C under stirring for assisting polymerization and condensation reactions. Finally, a gel-like yellowish material was obtained. After drying at 110 °C for 17 h, the solid powder became spongy. A heating step from room T to 400 °C in air was subsequently applied, where self-ignition took place at ∼350 °C and the material was kept at 400 °C for 30 min. After grinding, the resulting solid was calcined (static air) in an oven at 600 °C for 10 h to eliminate all the organic residues from the synthesis procedure. The $Pt/Ce_{1-x}La_xO_{2-\delta}$ catalysts were synthesized by the wet impregnation method. A given amount of aqueous solution of

$H_2PtCl_6 \cdot 6H_2O$ (Aldrich) corresponding to 0.5 wt% Pt metal loading was used to impregnate the support in powder form at 70 °C for 4 h. The resulting slurry was dried overnight at 120 °C and stored for further use.

2.2. Catalyst characterization

2.2.1. CO temperature-programmed desorption (TPD) studies

CO-TPD experiments were carried out in a specially designed gas flow-system previously described [25]. The 0.5 wt% $Pt/Ce_{1-x}La_xO_{2-\delta}$ catalyst (0.5 g) was first calcined (20 vol% O_2/He) at 600 °C for 2 h followed by H_2 reduction (1 bar) at 300 °C for 2 h, and then heated to 500 °C in He flow (30 min). It was then cooled to 150 °C in He flow and the feed was then switched to a 2 vol% CO/He gas mixture for 30 min followed by cooling of reactor to 30 °C under CO/He flow, where it was kept at 30 °C for 15 min (CO chemisorption step). A switch to He flow was then made for 15 min, and the temperature of the catalyst was subsequently increased to 800 °C (30 NmL min^{-1}, β = 30 °C min^{-1}). The mass numbers (m/z) 2, 18, 28, 32, 44 were used for continuously monitoring H_2, H_2O, CO, O_2 and CO_2, respectively with *on line* mass spectrometer (MS). The MS signals were calibrated against 2 vol% CO/He ($m/z = 28$), 985 ppm CO_2/He ($m/z = 44$) and 0.3 vol% H_2/He ($m/z = 2$) standard gas mixtures. At the end of the CO-TPD run (MS signals reached their respective background values in He flow), the catalyst was cooled in He flow to 30 °C and the feed was then switched to 2 vol% O_2/He gas mixture (30 NmL min^{-1}) and the temperature was increased to 800 °C (β = 30 °C min^{-1}). Based on the formation of gaseous CO and CO_2, "carbon" deposits (g "C"/g_{cat}) formed during CO-TPD can be estimated.

2.2.2. HAADF-STEM studies

Platinum particle size distribution and a mean Pt particle size for the 0.5 wt% $Pt/Ce_{1-x}La_xO_{2-\delta}$ catalysts ($x = 0$, 0.2 and 1.0) were estimated using High Angle Annular Dark Field (HAADF) images obtained in a 200 kV JEM-2100J (Jeol Ltd.) transmission electron microscope equipped with an INCAx-Sight (Oxford Inc.) energy-dispersive X-ray spectroscopy. HAADF images were recorded with the microscope in STEM mode with a beam size of 1 nm and an inner collection angle of 68.5 mrad. The contrast in HAADF images is mainly due to differences in the atomic number (Z) of metal elements at constant thickness. Given that $Z_{Pt} = 78$, $Z_{La} = 57$ and $Z_{Ce} = 58$, the brighter regions in the HAADF images correspond to Pt particles. Samples were first calcined at 600 °C (20%O_2/He) for 2 h, followed by H_2 reduction (1 atm H_2) at 300 °C for 2 h.

2.2.3. Oxygen storage capacity (OSC) measurements

The H_2–O_2 pulse injection technique [26] was used to measure the oxygen storage capacity (μmol O g_{cat}^{-1}) of the 0.5 wt% $Pt/Ce_{1-x}La_xO_{2-\delta}$ catalysts in the 250–550 °C range. The concentration of the most reactive oxygen species (oxygen storage capacity, OSC), and that of total reactive oxygen in the solid (oxygen storage capacity complete, OSCC) are defined as reported elsewhere [27,28]. Prior to OSC measurements, the catalyst ($W = 0.1$ g) was treated in a 20 vol% O_2/He gas mixture at a given temperature ($T_{OSC} = 250$–550 °C) for 1 h. Details of the experimental protocol used for OSC measurements was previously reported [27,29].

2.2.4. ^{18}O transient isotopic exchange studies

Transient ^{18}O isotopic exchange experiments were performed over the best and worst performed 0.5 wt% $Pt/Ce_{1-x}La_xO_{2-\delta}$ catalysts ($x = 0.2$ and 0.8, respectively) toward the WGS reaction. Analysis of the obtained transient isotopic response curves according to the literature [30] allowed to compare the rate of surface oxygen exchange with gaseous oxygen in the two solids, thus to probe surface oxygen mobility in each solid, and relate this

to the rate of WGS *via* the "redox" pathway (see Section 2.5). The latter involves the reaction of adsorbed CO with surface lattice oxygen at the Pt-support interface. The transient ^{18}O isotopic exchange experiments were performed at 600 °C over a fresh pre-reduced (H$_2$, 300 °C/2 h) catalyst sample (W = 80 mg), following the gas delivery sequence: 10 vol% O$_2$/Ar (600 °C, 2 h) → Ar (600 °C, 20 min) → 10 vol% ^{18}O$_2$/Ar (600 °C, t) (97% ^{18}O, Marchall Isotopes Ltd.). The Ar gas purge was used to eliminate completely ^{16}O^{18}O(g) contribution from possible gas-phase exchange (^{16}O/^{18}O), at least at the important initial stage of the transients' evolution after switching to the ^{18}O$_2$/Ar gas mixture. The following parameters were used for the analysis of the transient ^{18}O isotopic exchange experiment [30]:

$$f_{34}(t) = \frac{^{16}O^{18}O}{\sum {^iO^jO}} \qquad (2)$$

$$a_g(t) = \frac{^{16}O^{18}O + 2\,^{18}O_2}{2\sum {^iO^jO}} \qquad (3)$$

$$\sum {^iO^jO} = {^{16}O_2} + {^{16}O^{18}O} + {^{18}O_2} \qquad (4)$$

where $a_g(t)$ is the ^{18}O-atom fraction in the gas-phase, $f_{34}(t)$ is the fraction of ^{16}O^{18}O formed in the gas-phase during the transient isotopic exchange ($0 < f_{34}(t) < 1$), and the sum in the left-hand side of Eq. (4) refers to the summation of the mole fractions of all three oxygen isotopic gaseous species present after the ^{18}O$_2$/Ar gas switch.

2.2.5. In situ UV–vis diffuse reflectance spectroscopy (UV–vis/DRS) studies

A Perkin Elmer Lambda 950 spectrometer (use of a scan speed of 100 nm min^{-1} and a slit width of 2.0 nm) equipped with a high-temperature/high-pressure temperature controllable DRS cell (Harrick, Praying Mantis) were used to *in situ* record spectra of 0.5 wt% Pt/Ce$_{1-x}$La$_x$O$_{2-\delta}$ solids in the 270–800 nm range. UV–vis/DR spectra of the solid were recorded in Ar gas flow (30 NmL min^{-1}) at 25 °C following *in situ* oxidation at 600 °C (10 vol% O$_2$/Ar for 1 h) and/or *in situ* reduction at 300 °C (20 vol% H$_2$/Ar for 1 h). The spectrum of the reference material used (fluorilon) was taken at 25 °C in Ar gas flow and this was subtracted from the spectrum of the solid recorded. In order to determine the absorption band due to PtO$_2$, the following experiment was performed. The reference material instead of being the fluorilon was the support of Pt alone (Ce$_{1-x}$La$_x$O$_{2-\delta}$). The spectrum of the reference material taken at 25 °C in Ar gas flow was subtracted from the spectrum of supported metal catalyst (*e.g.*, 0.5 wt% Pt/CeO$_2$) after following exactly the same gas pre-treatment. The reflectance signal from the sample (R_{sample}) was converted to pseudo-absorbance units using the Kubelka–Munk function, $F(R_\infty)$ according to the following Eqs. (5) and (6) [31,32]:

$$R_\infty = \frac{R_{sample}}{R_{ref}} \qquad (5)$$

$$F(R_\infty) = \frac{(1-R_\infty)^2}{2R_\infty} \qquad (6)$$

where R_{ref} is the reflectance of a reference material.

2.2.6. Raman studies

100 mg of each catalyst in powder form were pressed into a wafer disc and mounted by gold wiring on the sample supporter of a homemade *in situ* Raman cell [33]. The cell consists of a double-walled quartz-glass transparent tube furnace mounted on a *xyz* plate allowing it to be positioned on the optical table. The inner

furnace tube (23 mm o.d., 20 mm i.d. and 10 cm long) was kanthal wire-wound for heating the cell. The cell had gas inlet and outlet as well as a thermocouple sheath possessing a sample supporter at its tip. *In situ* Raman spectra were recorded at 300 °C under N$_2$ gas flow (15 mL min^{-1}). Prior to recording the Raman spectra, each catalyst sample was treated under 15 mL min^{-1} flow of N$_2$ gas for 2 h. The 488.0 nm line of a Spectra Physics Stabilite 2017 Ar$^+$ laser operated at 40 mW was used for exciting Raman vibrational modes. The incident light was slightly defocused in order to reduce sample irradiance. The scattered light was collected at 90° (horizontal scattering plane), analyzed with a 0.85 m Spex 1403 double monochromator, and detected by a −20 °C cooled RCA PMT interfaced with Labspec data acquisition software.

2.2.7. In situ diffuse reflectance infrared fourier transform spectroscopy (DRIFTS) studies

In situ DRIFT spectra following CO chemisorption were recorded using a Perkin-Elmer Frontier FT-IR spectrometer (128 scans per spectrum, resolution of 4 cm^{-1}, scan speed of 2 cm/s) equipped with a high-temperature/high-pressure temperature controllable DRIFTS cell (Harrick, Praying Mantis). The catalyst sample (~80 mg) in a very fine powder form was placed firmly into the ceramic cup of the DRIFTS cell and first calcined at 600 °C for 2 h (20 vol% O$_2$/He) followed by H$_2$ reduction (1 bar) at 300 °C for 2 h. The spectrum of the solid in Ar gas flow was then recorded at the desired temperature (25–400 °C), and subtracted from the spectrum of the solid recorded after 3 vol% CO/Ar gas treatment. DRIFT spectra when necessary were smoothed to remove high frequency noise and further analyzed using the software Spectrum10 for Windows.

2.3. Catalytic performance and kinetic studies

The experimental apparatus used (Micro-reactivity Pro, CSIC-Spain) was previously described in detail [34]. A saturator with temperature control and pressure monitoring was used for the addition and control of water concentration in the reaction feed gas stream. The liquid water stream was first passed through a coil evaporator and then mixed with other gases using a small (~3 mL) mixing chamber. The outlet feed gas stream from the reactor was then directed to a peltier cooling system in order to remove water and condensable reaction gas products before directed to a mass spectrometer (Baltzers Omnistar^{TM}) for *on line* measurement of H$_2$, CO, CO$_2$, CH$_4$ and any higher hydrocarbons or oxygenates which were not condensed. Prior to any measurements, the catalyst (0.5 g) was calcined at 600 °C (20 vol% O$_2$/He) for 2 h, and then reduced at 300 °C in H$_2$ (1 bar) for 2 h. The WGS reaction feed stream used in all experiments was 3 vol% CO/10 vol% H$_2$O/87 vol% He, and the total gas volume flow rate was 200 NmL min^{-1}, yielding a GHSV of ~40,000 h^{-1}. The catalytic performance of Pt/Ce$_{1-x}$La$_x$O$_{2-\delta}$ was evaluated in the 200–400 °C range based on the CO conversion achieved given by the following Eq. (7):

$$X_{CO}(\%) = \frac{(F_{CO}^{in} - F_{CO}^{out})}{F_{CO}^{in}} \times 100 \qquad (7)$$

where F_{CO}^{in} and F_{CO}^{out} are the molar flow rates (mols/s) of CO at the reactor inlet and outlet, respectively.

Measurements of the intrinsic kinetic rate ($X_{CO} \sim 8$–12%) of WGS at 250 °C were performed over Pt/Ce$_{1-x}$La$_x$O$_{2-\delta}$ (x = 0.0, 0.2, 0.5, 0.8 and 1.0) catalysts, where the kinetic rate per gram of catalyst (r_{CO}, mol/g$_{cat}$ s) was calculated using Eq. (8):

$$r_{CO}\left(\frac{mol}{g_{cat}\,s}\right) = X_{CO}\left(\frac{F}{W}\right) \qquad (8)$$

where F is the total molar flow rate (mols/s) of CO in the feed gas stream and W is the mass of catalyst (g) used. Arrhenius plots

for estimating the apparent activation energy of WGS were constructed on the basis of kinetic rates estimated in the 250–350 °C range. The intrinsic kinetic rate expressed per length of the perimeter, I_o (cm/g_{cat}) of Pt-support interface, R_{CO} (mol/cm s) was estimated on the basis of the following Eq. (9):

$$R_{CO}\left(\frac{mol}{cm\ s}\right) = \frac{r_{CO}(mol/g_{cat}\ s)}{I_o(cm/g_{cat})} = \frac{r_{CO}.V_{Pt}.\rho_{Pt}}{\pi.d_{Pt}.L_{Pt}} \quad (9)$$

where V_{Pt} is the volume of a hemi-spherical Pt nanoparticle (cm^3), ρ_{Pt} is the platinum metal density (21.3 g/cm^3), d_{Pt} is the mean Pt particle diameter (cm), and L_{Pt} is the Pt loading (g_{Pt}/g_{cat}) in the catalyst sample. External and intraparticle mass and heat transfer resistances were estimated according to the procedure, relationships and criteria used in a previous publication [22]. These were found to be negligible.

2.4. Characterization of "carbon" deposits during WGS reaction

The amount of "carbon" accumulated on the catalyst surface after 4 h and 70 h of continuous WGS at 325 °C, and its reactivity toward oxygen were studied according to the following procedure. After WGS reaction the catalyst was heated to 800 °C in He flow (He-TPSR) to remove adsorbed water, CO$_2$ and/or carbonaceous deposits that could thermally decompose in He flow. The reactor was then quickly cooled in He flow to room temperature, and the gas flow was switched to a 2 vol% O$_2$/He mixture for a temperature-programmed oxidation (TPO) experiment (β = 30 °C min^{-1}). The H$_2$, CO and CO$_2$ MS signals were monitored until they reached practically their respective baseline value.

Quantification of the H$_2$, CO and CO$_2$ signals was made using standard calibration gas mixtures in He diluent gas for H$_2$ (0.3 vol% H$_2$/He), CO (2 vol% CO/He) and CO$_2$ (985 ppm CO$_2$/He). These transient experiments were conducted in a specially designed gas flow-system described elsewhere [25].

2.5. Probing the "redox" mechanism of WGS reaction

^{18}O/^{16}O isotopic exchange was first conducted at 600 °C (Section 2.2.4) using a catalyst sample of 0.083 g. In particular, the sample was first pre-treated in 10 vol% ^{18}O$_2$/Ar (97% ^{18}O, Marchall Isotopes Ltd.) at 600 °C for 30 min, purged in Ar gas flow and cooled to 80 °C. The feed was then switched to H$_2$ (1 bar) at 80 °C for 20 min in order to reduce only PtO$_x$ to Pt°. Following this gas treatment, the catalyst was then heated from 80 to 250 °C in Ar flow, and then exposed to the WGS reaction feed stream (3 vol% CO/10 vol% H$_2$O/Ar; 100 NmL/min). The mass numbers (m/z) 2 (H$_2$), 28 (C^{16}O), 44 (C^{16}O$_2$), 46 (C^{16}O^{18}O) and 48 (C^{18}O$_2$) in the mass spectrometer were continuously monitored under WGS reaction conditions.

3. Results and discussion

3.1. Catalyst characterization

3.1.1. Structural and textural properties of supports

According to previous studies [35–41], the citrate sol–gel method can lead to the formation of Ce$_{1-x}$La$_x$O$_{2-\delta}$ solid solution for x values close to 52 at.%. For the present Ce$_{0.2}$La$_{0.8}$O$_{2-\delta}$ solid, no diffraction peaks due to La$_2$O$_3$ were observed suggesting that the wt% lanthana phase (ca. <5 wt%) and its mean primary crystal size (ca. <4.0 nm) were out of the detection limit of XRD. Based on the FWHM of the diffraction line (1 1 1) (XRD studies) and the Scherrer equation [42], the mean primary crystal size was estimated: 19.5, 7.7, 4.6, 3.3 and 22.6 nm for CeO$_2$, Ce$_{0.8}$La$_{0.2}$O$_{2-\delta}$, Ce$_{0.5}$La$_{0.5}$O$_{2-\delta}$, Ce$_{0.2}$La$_{0.8}$O$_{2-\delta}$ and La$_2$O$_3$ solids, respectively [35]. It is seen that

the particle size of Ce$_{1-x}$La$_x$O$_{2-\delta}$ (x = 0.2, 0.5 and 0.8) is significantly smaller than that of single CeO$_2$ and La$_2$O$_3$ metal oxides.

The specific surface areas (SSA, m^{2}g^{-1}) of CeO$_2$, Ce$_{0.8}$La$_{0.2}$O$_{2-\delta}$, Ce$_{0.5}$La$_{0.5}$O$_{2-\delta}$, Ce$_{0.2}$La$_{0.8}$O$_{2-\delta}$ and La$_2$O$_3$ were 14.0, 42.0, 22.0, 14.0 and 7.0 m^{2}g^{-1}, respectively [35]. The mean pores diameter of the present Ce$_{1-x}$La$_x$O$_{2-\delta}$ solids was in the 4.1–9.3 nm range (mesoporous materials). These results are similar to those recently reported by Reddy et al. [43] in studying Ce$_{1-x}$La$_x$O$_{2-\delta}$ synthesized by a modified co-precipitation method, where after adding 20 at.% La^{3+} in ceria an increase in the SSA by a factor of 1.6 was obtained. Krishna et al. [44] using Raman spectroscopy showed that doping of ceria with La^{3+} shifted the sintering process by more than 100 °C and improved also its SSA (m^{2}g^{-1}).

3.1.2. Pt dispersion and mean particle size

3.1.2.1. HAADF/STEM studies. Fig. 1 shows high angle annular dark field (HAADF) images (STEM mode) obtained over the 0.5 wt% Pt/CeO$_2$ catalyst after calcination followed by hydrogen reduction procedures (Section 2.2.2). Pt/CeO$_2$ is composed of CeO$_2$ particles with size between 5 and 40 nm forming agglomerates (Fig. 1a). Ceria agglomerates as large as 0.5 μm were detected. It was found that in the case of small agglomerates ceria particles are randomly stacked together, whereas larger agglomerates are well ordered forming sheets. The brighter regions in the image of Fig. 1a correspond to thicker regions in the sample, whereas darker regions correspond to pores. Fig. 1b shows Pt nanoparticles (small bright spots) homogeneously distributed on CeO$_2$, whereas Fig. 1c shows the estimated Pt particle size distribution obtained after counting 200 particles. A mean Pt particle size of 1.2 (±0.3 s.d.) nm was estimated. HAADF/STEM images were also obtained on 0.5 wt% Pt/La$_2$O$_3$ [23] and 0.5 wt% Pt/Ce$_{0.8}$La$_{0.2}$O$_2$ (not shown here), where nanoparticles of Ce$_{0.8}$La$_{0.2}$O$_2$ between 5 and 15 nm forming agglomerates of 50–200 nm (smaller than on ceria) in size were observed. Based on EDX analyses performed in several regions of the Ce$_{0.8}$La$_{0.2}$O$_2$ sample, a mean Ce:La atom ratio of 81:19 with a s.d. of 2% was obtained, in excellent agreement with the nominal composition used in the synthesis. Maximum and minimum Ce:La atom ratios of 85:15 and 77:23 were measured, result that proves that no metal oxide segregation took place in the sample. A mean Pt particle size of 1.0 ± 0.2 nm was estimated for the 0.5 wt% Pt/Ce$_{0.8}$La$_{0.2}$O$_2$ catalyst. This is in good agreement with that estimated based on H$_2$ chemisorption performed at 25 °C using 0.3 vol% H$_2$/He for 15 min, followed by TPD in He flow. The latter hydrogen adsorption conditions proved to minimize hydrogen spillover on Pt/CeO$_2$. In our previous work [22], HAADF/STEM studies performed on 0.1 and 0.6 wt% Pt/CeO$_2$ catalysts, the ceria support being a commercial one with low SSA (5.6 m^2/g), revealed mean Pt particle sizes of 1.2 and 2.5 nm, respectively. These results illustrate that ceria synthesized by the citrate sol–gel method resulted in SSA (m^2/g^{-1}) and pores structures for the Ce$_{1-x}$La$_x$O$_{2-\delta}$ solids which positively influenced the stabilization of high Pt dispersions after using 0.5 wt% Pt loading and following calcination (20 vol% O$_2$/He) at 600 °C and reduction (H$_2$, 1 bar) at 300 °C.

Table 1
Dispersion of Pt (D, %) and Pt mean particle size (d_{Pt}, nm) estimated from HAADF/STEM and H$_2$ chemisorption followed by TPD studies.

0.5 wt% Pt/support	D (%)	d_{Pt} (nm)[a]	d_{Pt} (nm)[b]
CeO$_2$	92[b]	1.6	1.2 (±0.3 s.d.)
Ce$_{0.8}$La$_{0.2}$O$_{2-\delta}$	100[b]	1.2	1.0 (±0.2 s.d.)
Ce$_{0.5}$La$_{0.5}$O$_{2-\delta}$	85[a]	1.3	–
Ce$_{0.2}$La$_{0.8}$O$_{2-\delta}$	78[a]	1.4	–
La$_2$O$_3$	100[b]	–	1.0 (±0.3 s.d.)

[a] 0.3 vol% H$_2$/He chemisorption at 25 °C for 30 min; D (%) = 1.1/d_{Pt} (nm) × 100.
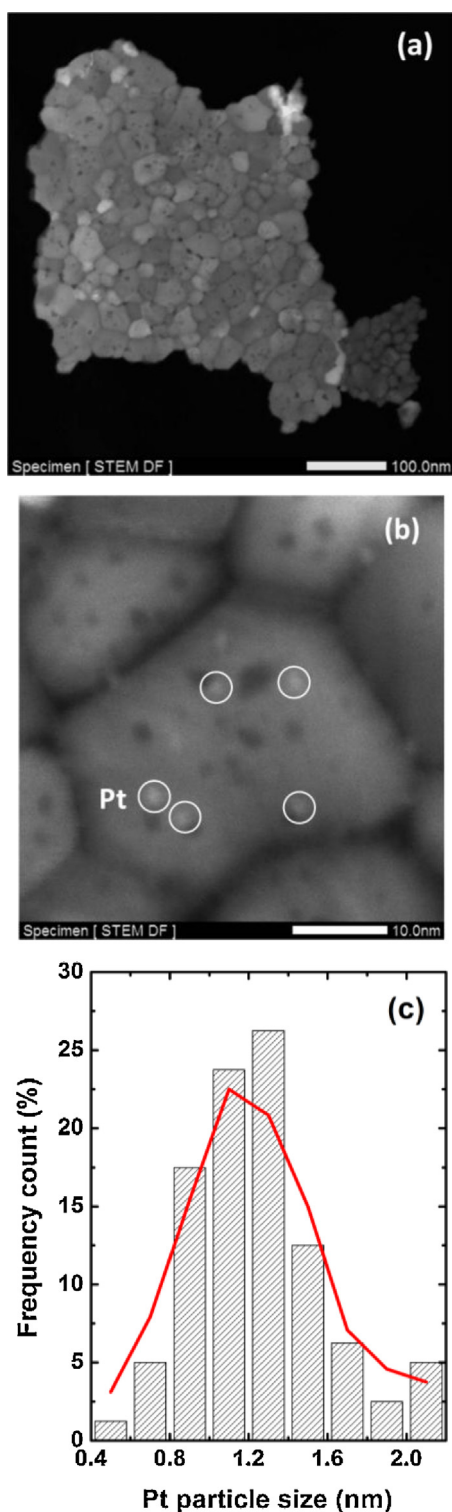[b] According to HAADF/STEM studies.

Fig. 2. Effect of support chemical composition on the conversion of CO (X_{CO}, %) as function of WGS reaction temperature obtained over 0.5 wt% $Pt/Ce_{1-x}La_xO_{2-\delta}$ (x = 0.0, 0.2, 0.5, 0.8 and 1.0) catalysts. Feed gas composition: $3\%CO/10\%H_2O/He$; GHSV = 40,000 h^{-1}.

result obtained on Pt/CeO_2 and $Pt/Ce_{0.8}La_{0.2}O_{2-\delta}$ catalysts (see Table 1).

3.2. Catalytic performance and kinetic studies

Fig. 2 presents catalytic performance results in terms of CO conversion (X_{CO}, %) as a function of the WGS reaction temperature for the 0.5 wt% $Pt/Ce_{1-x}La_xO_{2-\delta}$ (x = 0.0, 0.2, 0.5, 0.8 and 1.0) series of catalysts. It is first noted that no CH_4 was formed within the whole temperature range of 200–400 °C investigated, an important result which shows that these catalysts do not promote the undesirable reaction: $CO + 3H_2 \leftrightarrows CH_4 + H_2O$. It is seen that doping of ceria support with La^{3+} at the level of 20 at.% improves significantly the WGS catalytic performance, especially in the 275–350 °C range, where at 275 °C the X_{CO} increases by a factor of 1.4. On the other hand, by further increasing the La^{3+}-content to 50–80 at.% a significant decrease in X_{CO} is observed. In particular, at 275 °C the CO conversion decreased by a factor of 3.2 after increasing the La^{3+}-content from 20 to 80 at.% La^{3+} in the ceria support.

The apparent activation energy (E_{app}) of WGS reaction related to the $Pt/Ce_{0.8}La_{0.2}O_{2-\delta}$ and $Pt/Ce_{0.2}La_{0.8}O_{2-\delta}$ catalysts, which were found to exhibit the best and worst catalytic performance, respectively (Fig. 2) was estimated based on kinetic rate measurements ($X_{CO} < 15\%$) in the 250–350 °C range ($3\%CO/10\%H_2O/He$). This was found to be 18.8 (±0.3) and 21.0 (±0.2) kcal mol^{-1}, respectively for the $Pt/Ce_{0.8}La_{0.2}O_{2-\delta}$ and $Pt/Ce_{0.2}La_{0.8}O_{2-\delta}$ solids. Kinetic rate measurements of the WGS reaction were also performed over the series of $Pt/Ce_{1-x}La_xO_{2-\delta}$ catalysts at 250 °C. Specific kinetic rates obtained expressed per gram of catalyst, r_{CO} ($\mu mol\,g_{cat}^{-1}\,s^{-1}$), and per length of the perimeter of $Pt-Ce_{1-x}La_xO_{2-\delta}$ interface, R_{CO} ($\mu mol\,cm^{-1}\,s^{-1}$) are reported in Table 2. The length of the perimeter of Pt-support interface (I_o, cm/s) was also provided in Table 2. It is observed that r_{CO} depends strongly on the Ce/La atom ratio. For example, r_{CO} was increased by a factor of four going from $Pt/Ce_{0.2}La_{0.8}O_{2-\delta}$ (0.8 $\mu mol\,g_{cat}^{-1}\,s^{-1}$) to $Pt/Ce_{0.8}La_{0.2}O_{2-\delta}$ (3.2 $\mu mol\,g_{cat}^{-1}\,s^{-1}$). The supported Pt with high La^{3+}-content (50–80 at.%) presents r_{CO} values in the 0.8–1.3 $\mu mol\,g_{cat}^{-1}\,s^{-1}$ range. On the other hand, the specific kinetic rate of WGS reaction per length of perimeter of Pt-support interface, R_{CO} was found to present the largest value in the case of $Pt/Ce_{0.8}La_{0.2}O_{2-\delta}$ (1.15×10^{-11} $\mu mol\,cm^{-1}\,s^{-1}$) and the lowest one in the case of Pt/La_2O_3 (4.3×10^{-12} $\mu mol\,cm^{-1}\,s^{-1}$). Since these two catalysts have practically the same I_o value (Table 2), where the number of Pt sites per cm (Pt-support interface) is slightly only modified

Fig. 1. HAADF images (STEM mode) (a and b) and Pt particle size distribution (c) obtained over 0.5 wt% Pt/CeO_2 catalyst following 20 vol% O_2/He gas treatment at 600 °C for 2 h and reduction in H_2 (1 bar) at 300 °C for 2 h.

Table 1 reports the dispersion (D, %) and mean particle size of Pt (d_{Pt}, nm) of all $Pt/Ce_{1-x}La_xO_{2-\delta}$ (x = 0.0, 0.2, 0.5, 0.8 and 1.0) catalysts. In the case of $Pt/Ce_{0.5}La_{0.5}O_{2-\delta}$ and $Pt/Ce_{0.2}La_{0.8}O_{2-\delta}$ solids, these parameters were evaluated on the basis of H_2 chemisorption/TPD studies previously mentioned. This procedure was in good agreement with the HAADF/STEM
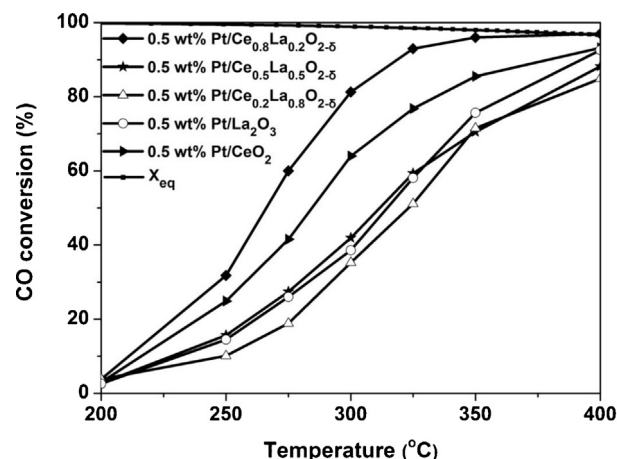
Table 2
Effect of Ce/La atom ratio on the specific kinetic rate of WGS reaction per gram of catalyst, r_{CO} (μmol g_{cat}^{-1} s^{-1}) and per total length of the perimeter of Pt-Ce$_{1-x}$La$_x$O$_{2-\delta}$ interface (I_o, cm g_{cat}^{-1}), R_{CO} (μmol cm^{-1} s^{-1}) at 250 °C (P_{CO} = 0.03 bar, P_{H_2O} = 0.1 bar, P_{He} = 0.87 bar).

0.5 wt% Pt/support	r_{CO} (μmol g_{cat}^{-1} s^{-1})	I_o (cm g_{cat}^{-1})	R_{CO} (μmol cm^{-1} s^{-1})
CeO$_2$	1.80	1.9×10^{11}	0.95×10^{-11}
Ce$_{0.8}$La$_{0.2}$O$_{2-\delta}$	3.20	2.8×10^{11}	1.15×10^{-11}
Ce$_{0.5}$La$_{0.5}$O$_{2-\delta}$	1.30	1.7×10^{11}	7.65×10^{-12}
Ce$_{0.2}$La$_{0.8}$O$_{2-\delta}$	0.80	1.4×10^{11}	5.70×10^{-12}
La$_2$O$_3$	1.20	2.8×10^{11}	4.30×10^{-12}

by the Pt particle size and metal oxide support composition (*e.g.*, Pt–Pt and $M^{n+} - O_L$ distances; M^{n+} and O_L is the support surface metal cation and lattice oxygen, respectively), it is implied that Pt/La$_2$O$_3$ must possess a smaller site reactivity (k) along the metal-support interface compared to Pt/Ce$_{0.8}$La$_{0.2}$O$_{2-\delta}$ catalyst. A recent mechanistic work reported from our laboratory on the WGS over the present Pt/Ce$_{1-x}$La$_x$O$_{2-\delta}$ solids [23] illustrated that the *active* reaction intermediates found in the C-path and H-path of WGS largely reside along the Pt-support interface. Based on this result and the discussion offered above, it is strongly indicated that the Ce/La atom ratio largely influences the reactivity of sites formed along the Pt nanoclusters (1.0–1.4 nm)-support interface.

3.3. Characterization of carbonaceous deposits following WGS

Fig. 3 presents CO$_2$ transient response curves obtained during TPO experiments (in terms of CO$_2$ formation rate) performed on Pt/Ce$_{0.8}$La$_{0.2}$O$_{2-\delta}$ and Pt/Ce$_{0.2}$La$_{0.8}$O$_{2-\delta}$ following 4 h of WGS reaction at 325 °C. In the case of Pt/Ce$_{0.8}$La$_{0.2}$O$_{2-\delta}$, two CO$_2$ peaks centered at 610 and 780 °C were obtained which correspond to the oxidation of two different kinds of "carbon" species formed under WGS reaction conditions. On the other hand, in the case of Pt/Ce$_{0.2}$La$_{0.8}$O$_{2-\delta}$ catalyst, only one large CO$_2$ peak centered at 800 °C is observed with shoulders at the rising and falling parts of the peak. The latter suggests the formation of less reactive "carbon" species. The total amount of "carbon" formed was found to be 1.8 and 14.5 μmol/g in the case of Pt/Ce$_{0.8}$La$_{0.2}$O$_{2-\delta}$ and Pt/Ce$_{0.2}$La$_{0.8}$O$_{2-\delta}$ catalysts, respectively. A similar TPO experiment performed on Pt/CeO$_2$ (not shown) resulted in 8.2 μmol "C"/g. This result illustrates that the lower catalytic activity observed on Pt/Ce$_{0.2}$La$_{0.8}$O$_{2-\delta}$ (Fig. 2) could be partially linked to the larger concentration of more refractory "carbon" deposits accumulated during WGS. It was reported [17] that deactivation of Pt/CeO$_2$ could arise from the formation of carbonates on the support surface,

thus blocking active catalytic sites according to a "redox" bifunctional mechanism [22,23]. It should be noted here that the CO$_2$ trace in Fig. 3 does not represent decomposition of carbonates to CO$_2$, since after WGS the catalyst was treated in He flow at 800 °C until the m/z = 44 signal in the MS reached its background value.

3.4. Catalyst activity with time on stream in WGS reaction

The stability behavior of Pt/Ce$_{0.8}$La$_{0.2}$O$_{2-\delta}$ and Pt/CeO$_2$ catalysts in the WGS reaction at 325 °C with time on stream (TOS) is illustrated in Fig. 4 up to 70 h on TOS. Pt/Ce$_{0.8}$La$_{0.2}$O$_{2-\delta}$ with the best catalyst activity (Fig. 2) was found to be very stable up to 50 h on TOS, whereas during the next 20 h the CO conversion decreased from 82 to only 74% (~10% decrease). On the other hand, Pt/CeO$_2$ shows a significant decrease in X_{CO} (%), namely from 80 to 45% (~44% decrease).

Fig. 5a shows transient response curves of CO$_2$ and H$_2$ obtained during He-TPSR performed over the Pt/Ce$_{0.8}$La$_{0.2}$O$_{2-\delta}$ catalyst following 70 h on TOS (stability test, Fig. 4). As shown in Fig. 5a, CO$_2$ evolution starts at about 250 °C with maximum at 510 °C and a shoulder in the 700–800 °C range, while a small H$_2$ evolution starts at about 325 °C with peak maximum at 570 °C and a small tail under the isothermal treatment of the catalyst at 800 °C. The amounts of CO$_2$ and H$_2$ formed were 303.6 and 3.1 μmol/g, respectively. In the case of Pt/CeO$_2$, the amounts of CO$_2$ and H$_2$ were found to be 14 and 0.1 μmol/g, respectively. These quantities reflect the large concentration of carbonates accumulating on the support during WGS and the small concentration of both formate (HCOO—) species accumulating on the support and H species on the Pt metal. It should be noted that —OH group decomposition into H$_2$(g) gas under He flow cannot be excluded. The justification of carbonate-type and formate species accumulating on the catalyst surface under WGS is based on recent work reported from our laboratory [23].
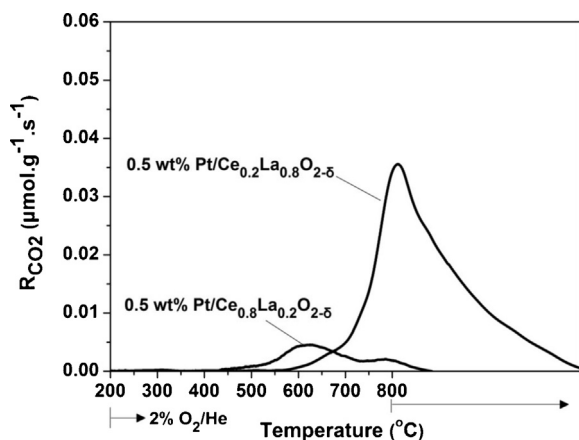

Fig. 3. CO$_2$ transient response traces obtained during TPO over 0.5 wt% Pt/Ce$_{0.8}$La$_{0.2}$O$_{2-\delta}$ and 0.5 wt% Pt/Ce$_{0.2}$La$_{0.8}$O$_{2-\delta}$ catalysts after 4 h of WGS reaction (3%CO/10%H$_2$O/He; GHSV = 40,000 h^{-1}) at 325 °C.
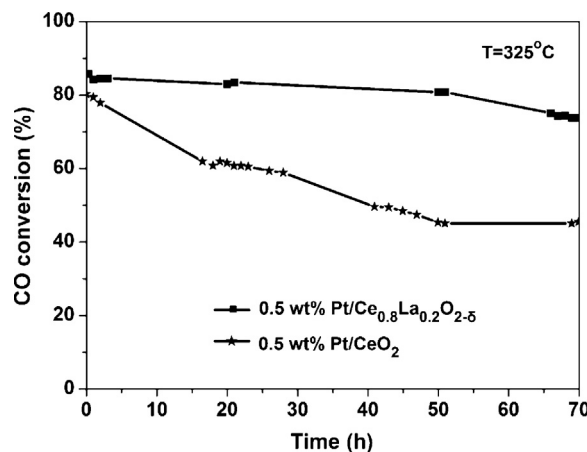

Fig. 4. Stability test obtained on 0.5 wt% Pt/Ce$_{0.8}$La$_{0.2}$O$_{2-\delta}$ and 0.5 wt% Pt/CeO$_2$ catalysts during 70 h on TOS in WGS reaction (3%CO/10%H$_2$O/He; GHSV = 40,000 h^{-1}) at 325 °C.
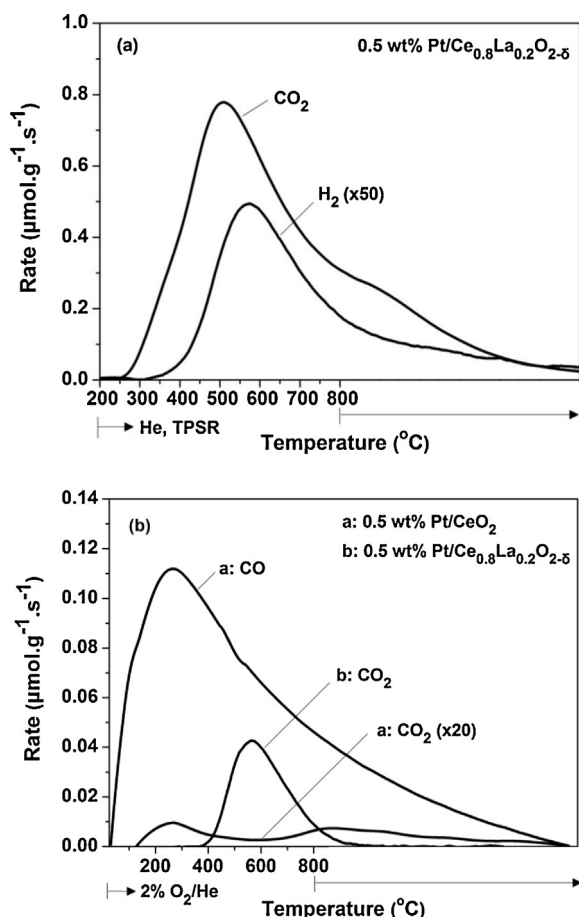
Fig. 5. (a) CO_2 and H_2 transient response curves obtained on 0.5 wt% $Pt/Ce_{0.8}La_{0.2}O_{2-\delta}$ during TPSR in He flow following WGS reaction for 70 h. (b) CO and CO_2 transient response curves obtained during TPO on 0.5 wt% $Pt/Ce_{0.8}La_{0.2}O_{2-\delta}$ and Pt/CeO_2 after TPSR in He flow.

Fig. 5b presents CO_2 and CO transient response curves obtained during TPO experiments following He-TPSR on Pt/CeO_2 and $Pt/Ce_{0.8}La_{0.2}O_{2-\delta}$ catalysts. The CO_2 response observed on $Pt/Ce_{0.8}La_{0.2}O_{2-\delta}$ (curve b) starts at higher temperatures compared to that observed during He-TPSR (250 vs. 400 °C), with a peak maximum at 565 °C. The amount of "carbon" removed from the surface during TPO was 10.2 μmol "C"/g. In the case of Pt/CeO_2, both CO_2 and CO response curves were obtained. CO evolution starts at ~30 °C showing a maximum at 270 °C and a large shoulder in the high-T side of the curve. A significantly smaller CO_2 response compared to that of CO was observed (curve a), where two CO_2 peaks appeared at 270 and 800 °C. The amount of "carbon" measured was 164.3 μmol "C"/g, to be compared to 10.2 μmol "C"/g for the $Pt/Ce_{0.8}La_{0.2}O_{2-\delta}$ catalyst. It is, therefore, clear that the best catalyst among the series of 0.5 wt% $Pt/Ce_{1-x}La_xO_{2-\delta}$ solids accumulates about 16 times lower amount of "carbon" compared to the solid with the second best catalytic performance (Fig. 2).

After comparing the TPO results for 4 h and 70 h on TOS (Figs. 3 and 5), it is now understood that one of the main reasons of Pt/CeO_2 deactivation (Fig. 4) is the accumulation of refractory "carbon" (164.3 vs. 10.2 μmol "C"/g). The catalytic performance of $Pt/Ce_{0.8}La_{0.2}O_{2-\delta}$ with TOS can be linked to the fact that this catalyst has the highest concentration of weak to medium basic sites among the series of $Pt/Ce_{1-x}La_xO_{2-\delta}$ solids [35], the latter result leading to the promotion of "carbon" gasification [45–47] as supported by the results of Fig. 5b.

3.5. Probing the catalytic activity vs. T behavior of $Pt/Ce_{1-x}La_xO_{2-\delta}$ solids

The following sections refer to the use of a variety of catalyst characterization techniques and spectroscopic methods which allowed gathering further fundamental information that reasonably explains the catalytic performance (Fig. 2) and kinetic results (Table 2) previously presented.

3.5.1. CO temperature-programmed desorption (CO-TPD)

Fig. 6a–d show CO-TPD profiles obtained on $Pt/Ce_{1-x}La_xO_{2-\delta}$ (x = 0.0, 0.2, 0.5 and 0.8) solids following CO chemisorption (Section 2.2.1). The CO-TPD profiles present desorption peaks of carbon monoxide, carbon dioxide and molecular hydrogen. The formation of CO_2 and H_2 could be due to the following reaction (Eq. (10)) [48,49]:

$$CO_M + OH_s \rightarrow CO_{2(g)} + \frac{1}{2}H_2(g) \tag{10}$$

where CO_M and OH_s refer to adsorbed CO on the metal (Pt) and hydroxyl group on the support adjacent to the M site (metal-support interface). Another possible route of CO_2 formation is the oxidation of adsorbed CO_M by surface lattice oxygen of support at the metal-support interface, according to the reaction (Eq. (11)) [50]:

$$CO_M + O_s \rightarrow CO_2(g) + (\square_s/e-) \tag{11}$$
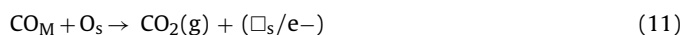
Furthermore, adsorbed CO on the metal surface can lead to the formation of CO_2 and carbon through the Boudouard reaction (Eq. (12)) (s: surface metal site) at temperatures usually higher than 100 °C [51]:

$$2CO\text{-}s \leftrightarrow CO_2(g) + C\text{-}s + s \tag{12}$$

Fig. 6e shows the transient response curve of CO_2 formation during TPO performed over the 0.5 wt% $Pt/Ce_{0.2}La_{0.8}O_{2-\delta}$ catalyst following CO-TPD (Fig. 6d, Section 2.2.1) in order to check whether Boudouard reaction (Eq. (12)) had occurred. The high temperature desorption peak of CO_2 (no CO was observed) shows the presence of a very refractive "carbon" species formed on the surface of the catalyst during CO-TPD. The amount of this "carbon" was 7.9 μmol/g, equivalent to $\theta_C = 0.45$ (based on the Pt_s surface atoms (μmol/g, Table 1).

The transient response curve of CO_2 obtained during CO-TPD in the case of Pt/CeO_2 (Fig. 6a) starts at ~60 °C and exhibits three discernable desorption peaks (T_M = 150, 260 and 730 °C) with a large shoulder on the rising part of the third peak. CO desorption results in two small and broad peaks with maxima at 153 and 260 °C, whereas H_2 desorption results in a broad peak centered at 540 °C and shoulders on its rising and falling parts. For $Pt/Ce_{0.8}La_{0.2}O_{2-\delta}$ (Fig. 6b) CO_2 evolution starts at 400 °C with peak maximum at 740 °C, and a shoulder on its rising part. A significant amount of H_2 desorbed resulting in two peaks with maxima at 170 and 470 °C (Fig. 6b). Desorption of CO presents two peaks at 263 °C (with a shoulder on its rising part) and 500 °C. In the case of $Pt/Ce_{0.5}La_{0.5}O_{2-\delta}$ (Fig. 6c), a large CO_2 peak is obtained starting at 550 °C with peak maximum at 790 °C. Small amounts of H_2 (T_M = 440 and 770 °C) and less CO (T_M = 350 and 450 °C) were also seen as depicted in Fig. 6c (see inset).

In the case of $Pt/Ce_{0.2}La_{0.8}O_{2-\delta}$ (Fig. 6d), a large CO_2 peak is obtained starting at 550 °C with peak maximum at 800 °C. Small amounts of CO (T_M = 335 °C) and H_2 (T_M = 370 °C) were also seen (see inset, Fig. 6d). It is interesting to note that the formation of hydrogen extends out to 800 °C as in all previous catalytic systems. Table 3 provides the quantities N_i (i = CO_2, CO and H_2) (μmol/g) of all gaseous products formed during CO-TPD conducted over the
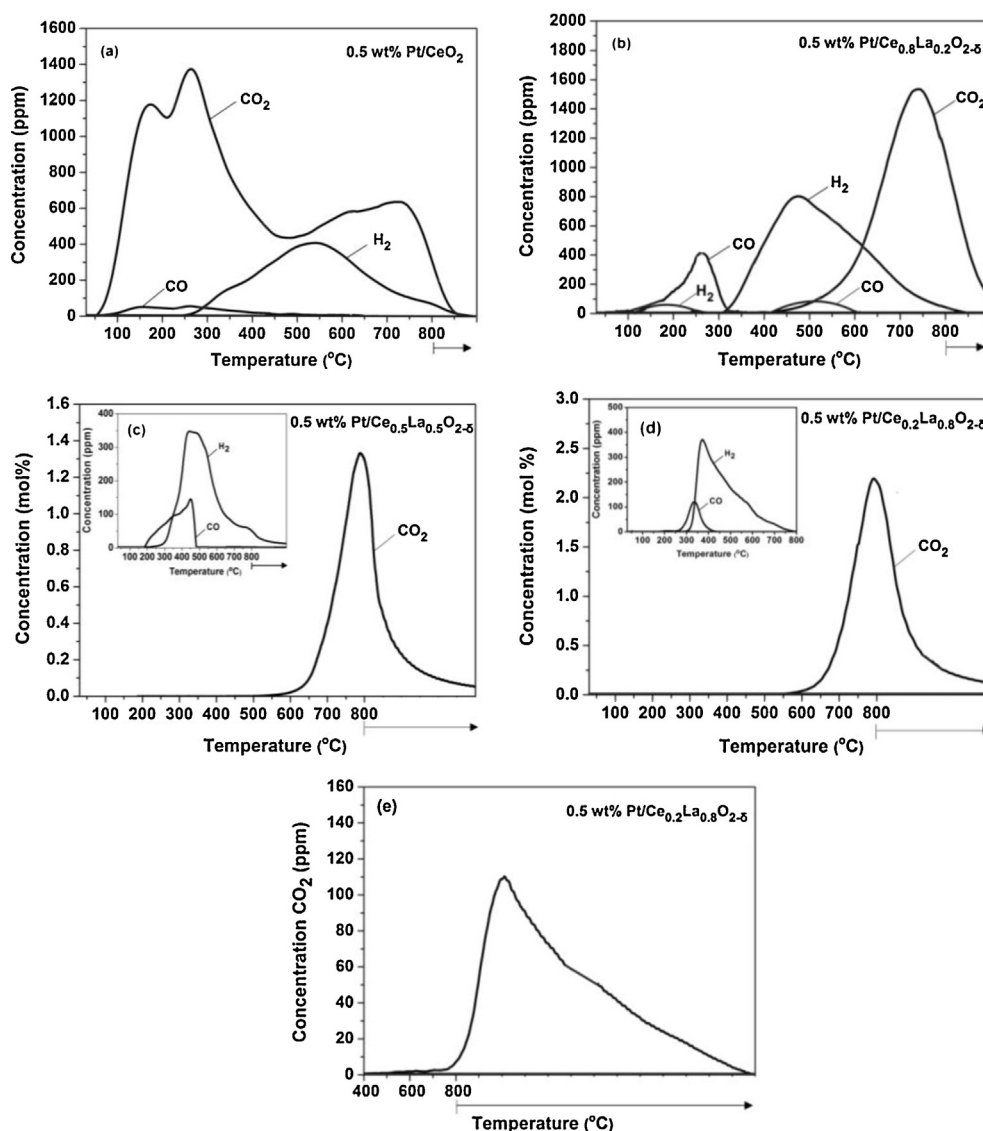
Fig. 6. CO, CO_2 and H_2 transient response curves obtained during CO-TPD performed on (a) 0.5 wt% Pt/CeO_2, (b) 0.5 wt% $Pt/Ce_{0.8}La_{0.2}O_{2-\delta}$, (c) 0.5 wt% $Pt/Ce_{0.5}La_{0.5}O_{2-\delta}$, and (d) 0.5 wt% $Pt/Ce_{0.2}La_{0.8}O_{2-\delta}$. (e) CO_2 response curve obtained during TPO on 0.5 wt% $Pt/Ce_{0.2}La_{0.8}O_{2-\delta}$ following CO-TPD. Chemisorption conditions: 2%CO/He (150 °C, 20 min) → cool in CO/He to 30 °C → He (30 °C, 15 min) → TPD in He flow to 800 °C ($\beta = 30$ °C min^{-1}).

five 0.5 wt% $Pt/Ce_{1-x}La_xO_{2-\delta}$ ($x = 0.0$, 0.2, 0.5, 0.8 and 1.0) catalytic systems. The amount of hydrogen formed on $Pt/Ce_{0.8}La_{0.2}O_{2-\delta}$ was found to be the largest among the other catalysts. This result shows that the reaction described by Eq. (10) proceeds to the largest extent over this catalyst, in agreement with the findings of our previous work [35], where H_2-TPR and TPD-NH_3 investigations revealed that $Ce_{0.8}La_{0.2}O_{2-\delta}$ presents the highest concentration of labile oxygen and surface acid sites (M–OH Brönsted acid sites). The opposite trend was obtained for the amount of desorbed CO_2, where reaction described by Eq. (11) takes place to a larger extent as the La^{3+}-content in the $Ce_{1-x}La_xO_{2-\delta}$ support increases. Also, after increasing the La^{3+}-content in the $Ce_{1-x}La_xO_{2-\delta}$ support causes CO_2 desorption to shift to higher temperatures, indicating that reaction of adsorbed CO with the lattice oxygen of support becomes a more activated step. On the other hand, CO_2-TPD experiments previously reported on the same $Ce_{1-x}La_xO_{2-\delta}$ support materials [35] showed that an increasing concentration of strong basic sites is formed as the La^{3+}-content in the support increases. These strong basic sites which are formed on the La^{3+}-rich support are likely responsible also for the high temperature desorption of CO_2 and the larger

amount of CO_2 formed compared to the La^{3+}-poor support content (higher Ce/La ratio).

Rieck and Bell [52] reported that the interaction of CO with La_2O_3-supported Pd is complex, since CO adsorbs on the support itself forming $La_2(CO_3)_3$ and oxy-carbonates, which are stable and decompose above 530 °C. This result is in harmony with the results of Fig. 6c and d, since as La^{3+}-content exceeds the value of ~50 at.% (Ce/La = 1/1, solubility limit), formation of pure lanthana is expected (see Section 3.1.1). In addition, according to the amount of CO_2 desorbed in the case of Pt/La_2O_3 (318.2 μmol/g, Table 3), this is equivalent to 12.4 monolayers of Pt_s ($\theta = 1$ corresponds to 12.4 μmol $Pt_{s/g}$, Table 1). The latter result strongly supports the view that during 2 vol% CO/He gas treatment of the catalyst at 150 °C (Section 2.2.1), most of CO chemisorption occurred on the La_2O_3 support. A similar conclusion is reached for the $Ce_{0.2}La_{0.8}O_{2-\delta}$ support. Based on these results, and those of He-TPSR following WGS reaction (Fig. 5a), the low activity of Pt supported on La_2O_3, $Ce_{0.5}La_{0.5}O_{2-\delta}$ and $Ce_{0.2}La_{0.8}O_{2-\delta}$ solids is also due to the accumulation of carbonates, the latter blocking active catalytic sites of WGS reaction pathways [23].

Table 3
Amounts of H_2, CO and CO_2 desorbed (μmol/g) and peak maximum desorption temperatures (T_M) estimated from CO-TPD experiments performed over the 0.5 wt% $Pt/Ce_{1-x}La_xO_{2-\delta}$ ($x = 0.0$, 0.2, 0.5, 0.8 and 1.0) catalysts following chemisorption at 150 °C (see Section 2.2.2).

0.5 wt% Pt/support	N_i (μmol/g)	T_M (°C)
CeO$_2$		
CO$_2$	44.1	150, 260, 730
CO	1.0	153, 260
H$_2$	10.6	540
Ce$_{0.8}$La$_{0.2}$O$_{2-\delta}$		
CO$_2$	23.9	740
CO	3.3	263, 500
H$_2$	17.8	170, 470
Ce$_{0.5}$La$_{0.5}$O$_{2-\delta}$		
CO$_2$	158.3	790
CO	1.8	350, 450
H$_2$	7.3	440, 770
Ce$_{0.2}$La$_{0.8}$O$_{2-\delta}$		
CO$_2$	301.9	800
CO	0.8	335
H$_2$	5.4	370
La$_2$O$_3$		
CO$_2$	318.2	800
CO	0.1	193
H$_2$	0.7	230

3.5.2. In situ DRIFTS studies

Fig. 7a presents *in situ* DRIFT spectra recorded on Pt/CeO$_2$ (A), Pt/Ce$_{0.8}$La$_{0.2}$O$_{2-\delta}$ (B), and Pt/La$_2$O$_3$ (C) catalysts after 30-min exposure to 3 vol% CO/Ar at 25 °C. All spectra show characteristic IR bands at 2085 and 2070 cm^{-1} corresponding to linear adsorbed CO on terrace and step sites of Pt° [22,53–56]. The IR band at 1835 cm^{-1} was recorded only on Pt/Ce$_{0.8}$La$_{0.2}$O$_{2-\delta}$ and it is associated with bridged-type adsorbed CO [22,55,56]. A small IR band recorded at 2045 cm^{-1} could be attributed to linear adsorbed CO on isolated platinum sites or on Pt sites along the Pt-support interface [57]. The main difference in the three spectra is the relative intensity of the IR bands recorded at 2085/2089 and 2070 cm^{-1}. In particular, after deconvolution and curve fitting (see inset, Fig. 7a), the integral band ratio I_{2070}/I_{2085} for Pt/Ce$_{0.8}$La$_{0.2}$O$_{2-\delta}$ is the lowest one (1.15) compared to Pt/La$_2$O$_3$ (1.58) and Pt/CeO$_2$ (2.43). It is therefore seen that the population of the two kinds of adsorbed linear CO is strongly influenced by the support chemical composition (Ce/La ratio). We have recently reported [23] that the linear adsorbed CO associated with the 2070 cm^{-1} IR band was the most reactive among the other linear-type CO species formed under WGS in the case of Pt/Ce$_{0.8}$La$_{0.2}$O$_{2-\delta}$ (Fig. 7c, ref. [23]). The results of Fig. 7a along with the catalytic and kinetic results presented in Section 3.2 could suggest that the surface coverage of this specific active CO species (IR band at 2070 cm^{-1}) may not be important for the rate-limiting step of WGS on Pt/Ce$_{1-x}$La$_x$O$_{2-\delta}$ solids.

Fig. 7b shows DRIFTS-CO spectra recorded on Pt/Ce$_{0.8}$La$_{0.2}$O$_{2-\delta}$ after CO chemisorption at 25 °C followed by temperature-programmed desorption in Ar flow up to 400 °C. The stepwise increase of catalyst temperature in Ar flow resulted in a progressive decrease in the integral IR band intensity accompanied by a red shift, which is consistent with a decrease in the dipole–dipole coupling between adsorbed CO due to a decrease in the surface coverage [58,59]. It is obvious that linear CO species are more thermally stable than bridged CO. An IR band recorded at 1985 cm^{-1} becomes visible at 100 °C, and this is likely associated to linear adsorbed CO on sites along the metal-support interface which are populated with increasing temperature in the 25–100 °C range [8,60]. Linear adsorbed CO still appears at 400 °C, in agreement with the CO-TPD results (Fig. 6b), where CO$_2$ formation (Eqs. (10)–(12)) does occur up to 800 °C. This result is important since it provides evidence
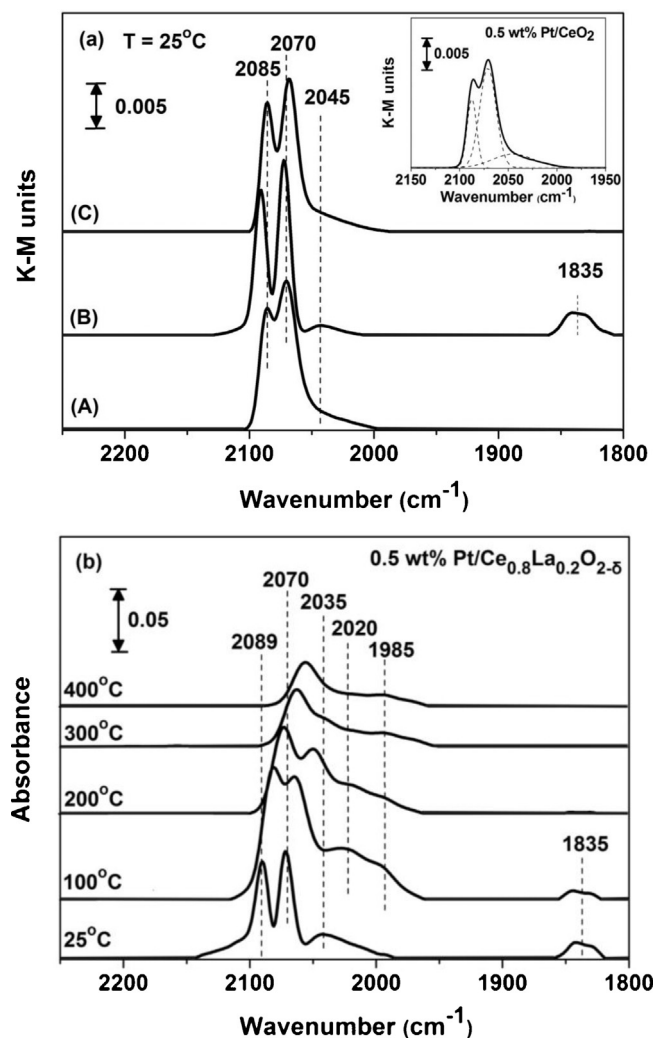

Fig. 7. (a) *In situ* DRIFTS spectra recorded at 25 °C in Ar flow over (A) 0.5 wt% Pt/CeO$_2$, (B) 0.5 wt% Pt/Ce$_{0.8}$La$_{0.2}$O$_{2-\delta}$, and (C) 0.5 wt% Pt/La$_2$O$_3$ catalysts following exposure to 3 vol% CO/Ar for 30 min at 25 °C. (b) *In situ* DRIFTS spectra recorded after 30 min of CO chemisorption (3 vol% CO/Ar) at 25 °C and after purge in Ar flow at temperatures in the 100–400 °C range over the 0.5 wt% Pt/Ce$_{0.8}$La$_{0.2}$O$_2$ catalyst.

for the formation of carbon *via* the Boudouard reaction (Eq. (12)), which is expected to occur at $T > 100$ °C [51]. The presence of carbon during WGS was also probed by the experimental study presented and discussed in the previous Sections 3.3 and 3.4.

3.5.3. In situ UV–vis diffuse reflectance spectroscopy (UV–vis/DRS)

UV–vis/DRS technique allows obtaining information on the coordination environment, metal ion oxidation states, and energy band gap of a metal oxide. It allows also obtaining oxidation states of a metal supported on metal oxide carriers. Furthermore, UV–vis/DRS can give information for solids of very small primary particle size (<4 nm), and low content (<1 wt%), where the XRD method is unsuccessful [61,62]. Fig. 8 presents UV–vis/DR spectra recorded on Ce$_{0.8}$La$_{0.2}$O$_{2-\delta}$ and 0.5 wt% Pt/Ce$_{0.8}$La$_{0.2}$O$_{2-\delta}$ (Fig. 8a) solids after calcination at 600 °C for 1 h (10 vol% O$_2$/Ar) or reduction at 300 °C for 1 h (20 vol% H$_2$/Ar) following calcination. In the case of calcination of support alone, two absorption bands were recorded at 280 and 325 nm due to the charge transfer from the O 2p to Ce^{4+} 4f orbital, and to inter-band transitions, respectively [44]. The spectra of supported Pt after calcination exhibit one additional absorption band in the 400–500 nm range
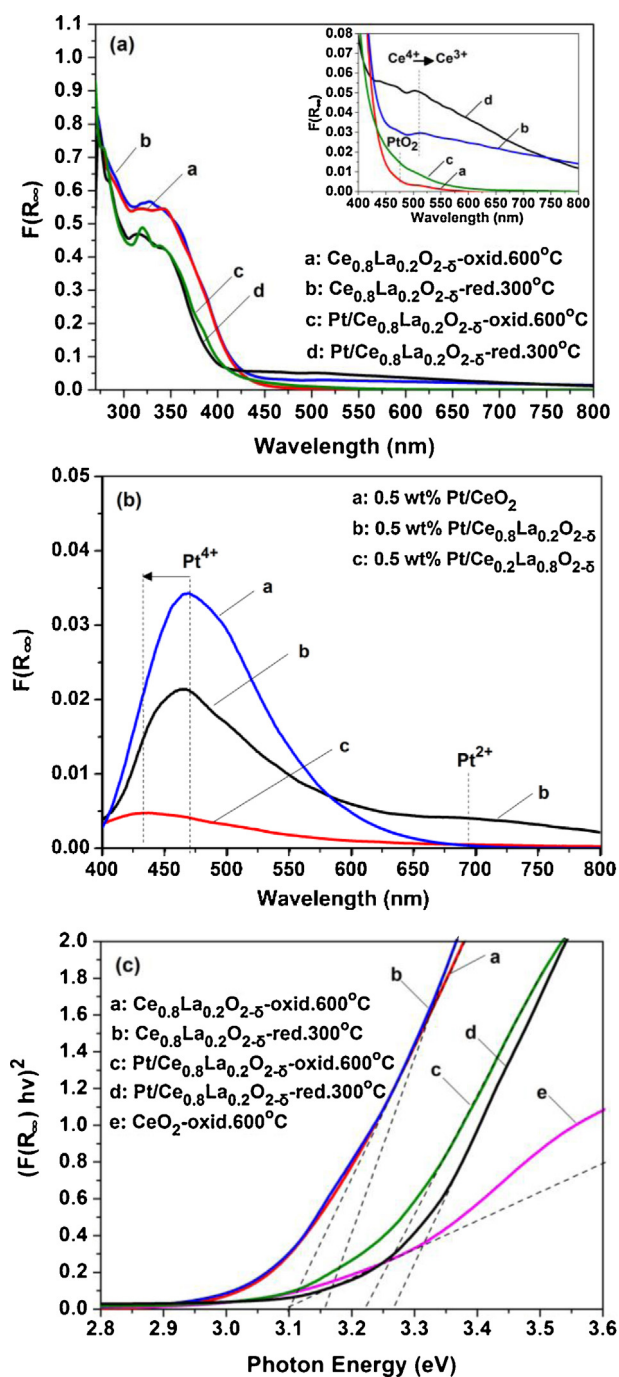
Fig. 8. UV–vis/DR spectra recorded on (a) $Ce_{0.8}La_{0.2}O_{2-\delta}$ and 0.5 wt% $Pt/Ce_{0.8}La_{0.2}O_{2-\delta}$ after oxidation (600 °C/1 h) and reduction (300 °C/1 h) and (b) on 0.5 wt% $Pt/Ce_{1-x}La_xO_{2-\delta}$ (x = 0.0, 0.2 and 0.8) after oxidation (600 °C/1 h). (c) Illustration of the method of estimating the energy band gap of CeO_2 and $Ce_{0.8}La_{0.2}O_{2-\delta}$ solids after oxidation and reduction pretreatments.

(Fig. 8a, inset), attributed to platinum oxide (d-d transitions of Pt) [63]. Fig. 8b shows UV–vis/DR spectra recorded on Pt/CeO_2, $Pt/Ce_{0.8}La_{0.2}O_{2-\delta}$ and $Pt/Ce_{0.2}La_{0.8}O_{2-\delta}$ catalysts after using the support ($Ce_{1-x}La_xO_{2-\delta}$) instead of fluorilon as a reference material. The spectra were collected after clacination at 600 °C for 1 h. In the case of Pt/CeO_2 and $Pt/Ce_{0.2}La_{0.8}O_{2-\delta}$ solids, one absorption band was observed at 470 and 430 nm, respectively. On the other hand, $Pt/Ce_{0.8}La_{0.2}O_{2-\delta}$ presents one absorption band centered at 468 nm and a small broad band in the 600–800 nm range. According to the literature [63–65], the absorption band in the 400–500 nm

range corresponds to Pt^{4+}, whereas that in the 600–800 nm range to Pt^{2+}. It has been reported [66] that by increasing the La_2O_3 content in the $Pt/CeO_2–La_2O_3–Al_2O_3$ system the maximum of absorption band recorded at 460 shifted to 506 nm. This shift is the result of the different types of electronic interactions between Pt and the support phase. In particular, a change in the coordination sphere of Pt (due to interactions developed because of the different support chemical composition, *e.g.* Ce/La ratio) results in a shift in the maximum of absorption band related to the d–d transitions of Pt. In the present work, it is obvious that as La^{3+}-content in the support increases, the band at 470 nm shifted to 430 nm, indicating different metal-support electronic interactions. It is pointed out that the catalyst which exhibits the best catalytic performance ($Pt/Ce_{0.8}La_{0.2}O_{2-\delta}$) presents the characteristic absorption band of Pt^{2+}. The latter shows that this catalyst is more resistant to oxidation. Thus, it could be suggested that Pt supported on $Ce_{0.8}La_{0.2}O_{2-\delta}$ is expected to be found in a more reduced state under WGS reaction conditions than if supported on CeO_2 or $Ce_{0.2}La_{0.8}O_{2-\delta}$. This in turn is expected to enhance CO chemisorption and H_2 formation rate. Also, during WGS reaction H_2O oxidizes Pt, and finally deactivation of the catalyst could occur (no ability of CO to adsorb). The better catalytic activity (Fig. 2) and stability (Fig. 4) exhibited by $Pt/Ce_{0.8}La_{0.2}O_{2-\delta}$ catalyst could be partly explained as due to this property (resistance of Pt to oxidation).

UV–vis/DR spectra recorded after reduction of the solids at 300 °C (following calcination at 600 °C) are shown in Fig. 8a (270–800 nm range, and in the inset graph (400–800 nm range)), where absorption bands at 540 nm are ascribed to $Ce^{4+} \rightarrow Ce^{3+}$ transitions [67,68]. These bands support the presence of inherent oxygen vacant sites in the solid, part of which was also formed after *in situ* hydrogen reduction at 300 °C. The band at 540 nm (Fig. 8a, inset) appears in the case of $Ce_{0.8}La_{0.2}O_{2-\delta}$, $Pt/Ce_{0.8}La_{0.2}O_{2-\delta}$ and $Pt/Ce_{0.2}La_{0.8}O_{2-\delta}$ (not shown) but not of $Ce_{0.2}La_{0.8}O_{2-\delta}$. These results show that reduction of $Ce_{0.8}La_{0.2}O_{2-\delta}$ alone or in the presence of Pt does occur at 300 °C, but not in the case $Ce_{0.2}La_{0.8}O_{2-\delta}$ which occurred at higher temperatures (*ca.* 500 °C) [35]. The better reducibility of $Ce_{0.8}La_{0.2}O_{2-\delta}$ support at low-temperatures is in agreement also with the higher OSC obtained (Section 3.5.5). The existence of vacant sites in $Ce_{0.8}La_{0.2}O_{2-\delta}$ was also verified by Raman Spectroscopy (Section 3.5.4).

In the case of supported metal catalysts after reduction, absorption in the 400–800 nm range was increased due to the surface plasmon resonance effect associated with metallic Pt nanoparticles. A similar observation was made by Yang et al. [69] on $Pt/TiO_2–SiO_2$. Based on this information, the higher intensity of absorption band in the 400–800 nm range observed in $Pt/Ce_{1-x}La_xO_{2-\delta}$ catalysts after reduction (Fig. 8a inset) is suggested to be due to both the reduction of support (540 nm) and the presence of Pt°.

The charge transfer between the fully occupied O 2p and the empty Ce 4f orbitals corresponds to the energy band gap of ceria [70]. The energy band gap estimation was performed by plotting the square root of Kubelka–Munk function multiplied by the photon energy ($[F(R_\infty)h\nu]^2$) against the photon energy ($h\nu$, eV) and extrapolating the linear part of the rising part of the curve to zero (Fig. 8c) [32,71,72]. CeO_2 is an n-type semiconductor with an energy band gap between 2.8 and 3.2 eV [73–75], whereas La_2O_3 is a p-type semiconductor with a higher band gap (4.3 eV) than CeO_2 [76]. The energy band gap of the present CeO_2 was found to be 3.09 eV. By increasing La^{3+} concentration in the $Ce_{1-x}La_xO_{2-\delta}$ solid results in an increase of the energy band gap to 3.34 eV for $Ce_{0.2}La_{0.8}O_{2-\delta}$ after calcination at 600 °C. This positive difference in energy band gap is due to effects of the presence of La^{3+} in CeO_2 (occupancy of electronic states), and likely also to the different mean crystallite size exhibited by the solid supports. For nanoparticles down to 7–8 nm (exciton Bohr radius), the energy band gap is modified because of quantum confinement effects, which typically

are measured by the blue shift of light absorbance [77]. According to Fig. 8c, the energy band gap of $Ce_{0.8}La_{0.2}O_{2-\delta}$ was found to be 3.10 and 3.15 eV after calcination at 600 °C and reduction at 300 °C, respectively. The $Ce_{0.2}La_{0.8}O_{2-\delta}$ and $Pt/Ce_{0.2}La_{0.8}O_{2-\delta}$ solids provided an energy band gap equal to 3.34 eV after calcination and reduction, whereas $Pt/Ce_{0.8}La_{0.2}O_{2-\delta}$ provided a band gap of 3.22 eV and 3.26 eV, respectively. It is seen that $Pt/Ce_{0.8}La_{0.2}O_{2-\delta}$ exhibits higher energy band gap values than its support alone. This result suggests for an electronic interaction between Pt and support, and is in agreement with the findings of Huang et al. [78] who reported that the energy band gap of Pt/TiO_2 increased after calcination compared to that of TiO_2 alone. In the case of the present $Pt/Ce_{0.8}La_{0.2}O_{2-\delta}$ catalyst, the energy band gap increased after reduction compared to that obtained following only calcination. This indicates that formation of oxygen vacant sites (as confirmed by Raman spectroscopy, OSC and H_2-TPR) affects the electronic states in the support. It is important to point out that the best catalytic performance was exhibited by the solid with the lowest energy band gap (3.26 eV) following calcination and reduction.

The CO-TPD (Fig. 6) and DRIFTS-CO (Fig. 7) studies point out that the metal-support interface largely influenced CO chemisorption properties (types of adsorbed CO and surface coverage) on Pt, which in turn influenced the rate of WGS reaction. The present UV–vis/DRS studies revealed that $Ce_{0.8}La_{0.2}O_{2-\delta}$ after loaded with 0.5 wt% Pt, calcined at 600 °C and then reduced at 300 °C exhibits the lowest energy band gap and the best WGS activity among the other supports. This result may suggest that electron flow from the $Ce_{0.8}La_{0.2}O_{2-\delta}$ support to the Pt nanoparticles becomes easier, result that could contribute to more favorable adsorption states of CO on Pt and along the Pt-support interface, thus enabling it to participate in the WGS reaction mechanism(s) with lower activation energy.

3.5.4. Raman studies

Raman spectra recorded on CeO_2 and $Ce_{0.8}La_{0.2}O_{2-\delta}$ under N_2 gas flow at 300 °C are shown in Fig. 9. The spectrum of CeO_2 presents a characteristic F_{2g} band at 458 cm^{-1} of the fluorite structure, which corresponds to the symmetric breathing mode of oxygen atoms around each Ce^{4+} cation [79,80]. The width and position of this Raman band is very sensitive to any structure disorder of the oxygen sub-lattice, since this vibration depends only on the oxygen movement [81]. In the present work (Fig. 9), this band is slightly red shifted (CeO_2) compared to the ideal 465 cm^{-1} value. The red shift is accounted by the elevated temperature (300 °C) and the presence of defects in the ceria lattice. A certain extent of defects is identified as a result of the observed weak and broad modes at 245
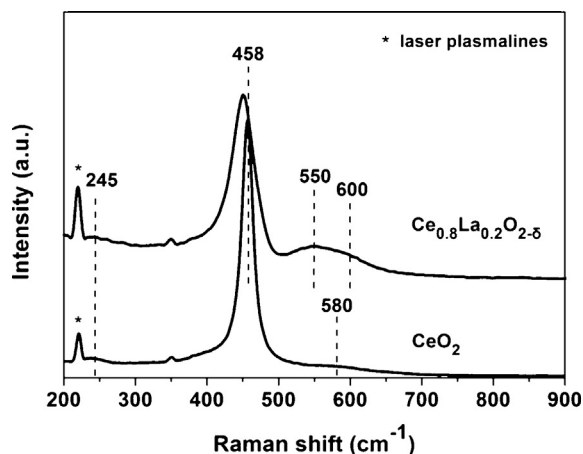
and 580 cm^{-1}, attributed to punctual defects in the ceria network. The weak band observed at ~245 cm^{-1} is assigned to leaking from relaxation of symmetry selection rules, due to the Raman inactive (IR-active) zone-center transverse optical (TO) mode. The presence of a weak band in the 580–600 cm^{-1} region is attributed to the existence of intrinsic oxygen vacancies in the oxide structure due to non stoichiometric composition [81–83]. Therefore, the present Raman results show the existence of Ce^{3+} and oxygen vacancies in ceria, and the band near 600 cm^{-1} is leaking from symmetry relaxation (lowering), and is due to the longitudinal optical (LO) vibrational mode of CeO_2.

In the case of $Ce_{0.8}La_{0.2}O_{2-\delta}$, Raman bands at 245, 452, 550 and 600 cm^{-1} were recorded. The existence of F_{2g} band (452 cm^{-1}) illustrates that $Ce_{0.8}La_{0.2}O_{2-\delta}$ exhibits global cubic fluorite structure. The F_{2g} band has lower intensity, the FWHM (full width half maximum) increased and shifted to a lower wavenumber (452 cm^{-1}) compared to pure ceria (458 cm^{-1}). Several studies [44,84,85] presented similar results. Yu Pikalova et al. [85] reported that the former shift depends on the effective radius of cation-dopant. In particular, doping of ceria with a larger in radius dopant than Ce^{4+} shifts the F_{2g} band to lower wavenumbers and *vice versa*. This change in the F_{2g} band of $Ce_{0.8}La_{0.2}O_{2-\delta}$ shows that La^{3+} was indeed incorporated in the ceria lattice as previously also mentioned (XRD studies); a shift in the diffraction peaks toward lower 2θ values was observed. The existence of the band at 550 cm^{-1} which is ascribed to oxygen vacancies confirms detailed XRD studies [81,82]. The intensity of this band allows to state that when ceria is doped with 20 at.% La^{3+} a larger concentration of O vacancies
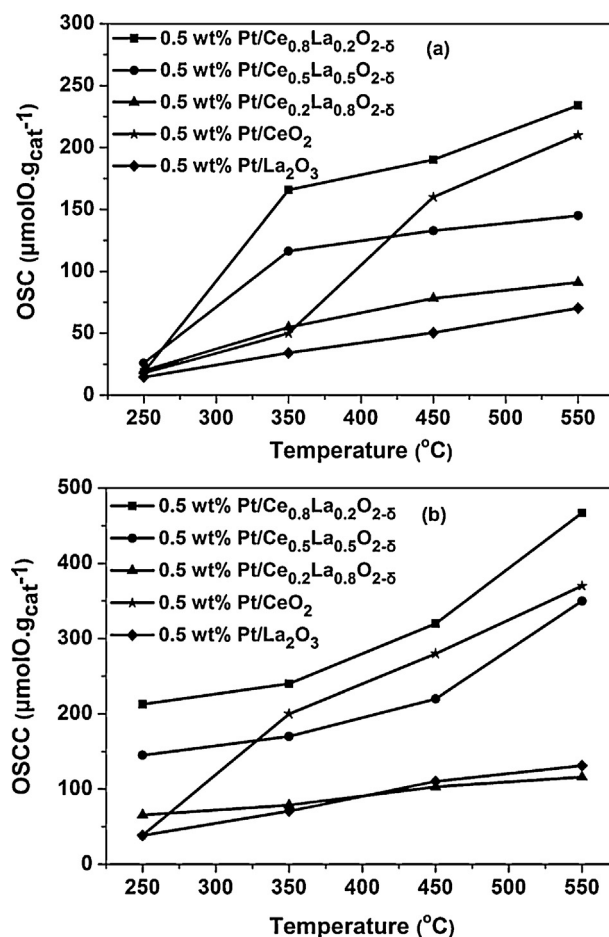

Fig. 10. (a) OSC and (b) OSCC (μmol O/g_{cat}) measured by O_2/H_2 pulses over 0.5 wt% $Pt/Ce_{1-x}La_xO_{2-\delta}$ ($x = 0.0, 0.2, 0.5, 0.8$ and 1.0) catalysts as a function of temperature.

Fig. 9. *In situ* Raman spectra recorded at 300 °C in N_2 gas flow on CeO_2 and $Ce_{0.8}La_{0.2}O_{2-\delta}$ solids.

is formed compared to pure CeO_2. The latter result is confirmed by OSC studies described in the next Section 3.5.5. In the case of $Ce_{0.5}La_{0.5}O_{2-\delta}$, the intensity of the band at $550\,cm^{-1}$ was lower than in $Ce_{0.8}La_{0.2}O_{2-\delta}$ and slightly lower than in pure CeO_2. This result is in agreement with the OSCC results observed in the 350–550 °C range (Fig. 10b) to be presented and discussed in the following Section 3.5.5.

3.5.5. Oxygen storage capacity, OSC

Fig. 10 presents OSC (Fig. 10a) and OSCC (Fig. 10b) (μmol $O\,g_{cat}^{-1}$) measured in the 0.5 wt% $Pt/Ce_{1-x}La_xO_{2-\delta}$ solids in the 250–550 °C range. It is seen that both OSC and OSCC increase with increasing temperature due to the temperature dependence of the rate of reaction of hydrogen with lattice oxygen, and to the increasing participation of oxygen diffusion from the bulk to the surface of the solid. It is shown that the OSC and OSCC measured on $Pt/Ce_{0.8}La_{0.2}O_{2-\delta}$ is the highest among the other solids. In particular, the OSC at 350 °C is larger by a factor of 4.2 and 4.5, respectively compared to pure ceria and lanthana. Similar results were obtained by Reddy et al. [43] on CeO_2 and $Ce_{0.8}La_{0.2}O_{2-\delta}$, where an increase of OSC by a factor of 5.5 was obtained. Katta et al. [86] reported OSC values of 40, 162 and 225 μmol $O\,g_{cat}^{-1}$, respectively, on pure CeO_2, CeO_2–ZrO_2 (1:1 mol/mol) and CeO_2–La_2O_3 (8:2 mol/mol) solid solutions, all prepared by a modified co-precipitation method. These results indicated the significant effect of Zr^{4+}- and La^{3+}-dopants in ceria in enhancing the concentration of oxygen vacancies. It is seen that in the 450–550 °C range, where bulk oxygen mobility becomes important in the measurement of OSCC, ceria appears to have larger oxygen storage capacity values than La^{3+}-doped ceria with La^{3+}-content larger than 50 at.%. This result is due to the fact that by increasing the La^{3+}-content the possibility of forming a stable vacancy-dopant cation association that limits the number of mobile vacancies increases [39]. Thus, the ability of oxygen mobility is limited. The present OSC results are in excellent agreement with those reported on $Ce_{1-x}La_xO_{2-\delta}$ prepared by sol–gel methods [39]. It was reported [39] that beyond the limit of 18 at.% La^{3+}-dopant concentration in ceria the OSC dropped. By exceeding the solubility limit ($\sim$52 at.%) of La^{3+} in CeO_2, the remaining lanthanum is expected to be found as La_2O_3, which exhibits low OSC (Fig. 10). Thus, based on these two reasons the OSC behavior of $Ce_{0.2}La_{0.8}O_{2-\delta}$ (80 at.% La^{3+}) can be justified (Fig. 10).

$Ce_{0.8}La_{0.2}O_{2-\delta}$ presents the highest rate of reduction by hydrogen at low temperatures [35], and the highest OSC (Fig. 10) among the $Ce_{1-x}La_xO_{2-\delta}$ solids investigated. The availability of labile oxygen within a reactive zone around the Pt nanoparticles can lead to a higher rate of CO_2 formation during WGS, leaving behind an oxygen vacant site (reduced support surface) [23]. Water can then re-oxidize the reduced support surface within this reactive zone forming di-hydrogen ("redox" mechanism of WGS). This mechanism was reported [22–24] to operate on $Ce_{1-x}La_xO_{2-\delta}$ ($x = 0.0, 0.2$ and 1.0) and $Ce_{0.5}Zr_{0.5}O_2$-supported Pt catalysts in the 250–300 °C range. The effect of Ce/La atom ratio on this important kinetic aspect of WGS is elaborated in the next Section 3.5.6. Panagiotopoulou and Kondarides [87] reported enhanced WGS activity on Pt/TiO_2 after increasing the reducibility of titania support by chemical promotion.

3.5.6. Effect of Ce/La ratio on the "redox" mechanism in WGS over $Pt/Ce_{1-x}La_xO_{2-\delta}$

Fig. 11 presents transient isotopic response curves of $C^{18}O_2$, $C^{16}O^{18}O$ and $C^{16}O_2$ obtained under the $C^{16}O/H_2O/Ar$ feed gas stream according to the experiment described in Section 2.5 over the $Pt/Ce_{0.8}La_{0.2}O_{2-\delta}$ (Fig. 11a) and $Pt/Ce_{0.2}La_{0.8}O_{2-\delta}$ (Fig. 11b) catalysts. The purpose of this experiment was to probe the effect of Ce/La atom ratio in support composition on the extent of participation of the "redox" mechanism in WGS over the
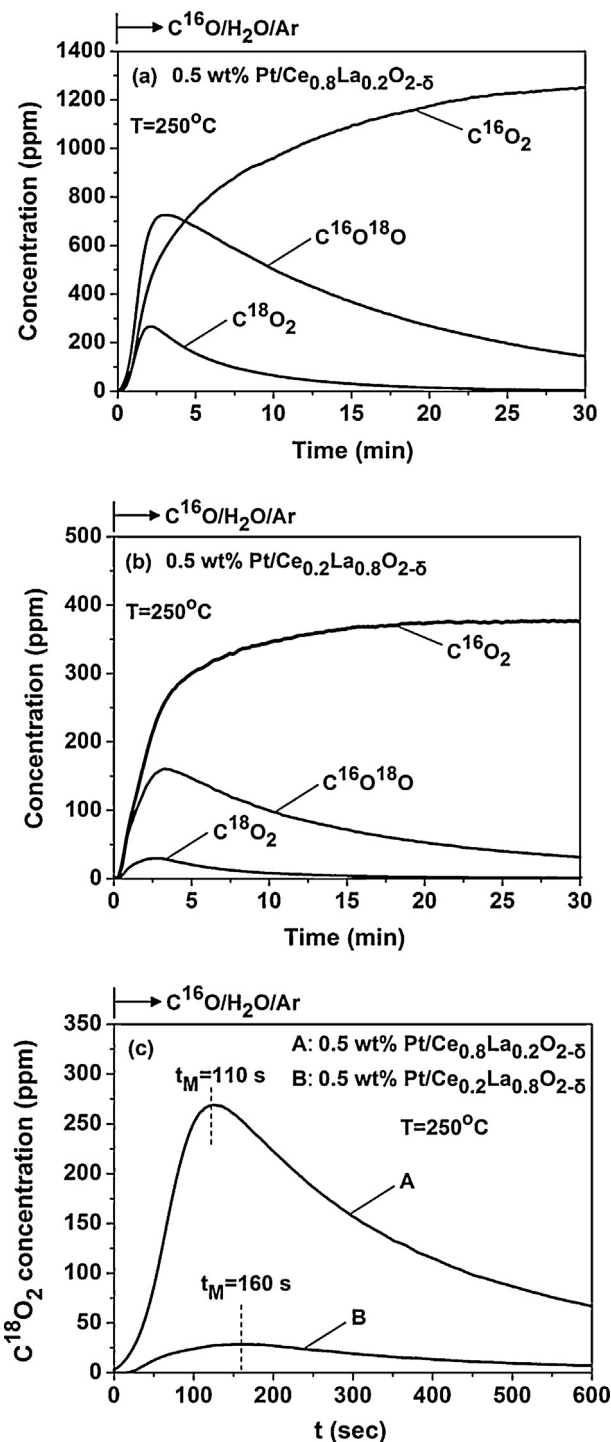

Fig. 11. Transient response curves of $C^{16}O_2$, $C^{16}O^{18}O$ and $C^{18}O_2$ obtained over the 0.5 wt% $Pt/Ce_{0.8}La_{0.2}O_{2-\delta}$ (a) and 0.5 wt% $Pt/Ce_{0.2}La_{0.8}O_{2-\delta}$ (b) catalysts at 250 °C under WGS reaction according to the following gas delivery sequence: 10 vol% $^{18}O_2/Ar$ (600 °C, 30 min) → cool in Ar flow to 80 °C → H_2 (30 min, 80 °C) → Ar increase T to 250 °C → $C^{16}O/H_2O/Ar$ (250 °C, t).

$Ce_{1-x}La_xO_{2-\delta}$-supported Pt catalyst [23]. The position in time, peak maximum and shape of the transient response curves of $C^{18}O_2$ and $C^{16}O^{18}O$ at the initial stage of the transient, reflect largely the kinetics of participation of lattice ^{18}O in the WGS reaction via the "redox" route. It is illustrated that in the case of Pt supported on $Ce_{0.8}La_{0.2}O_{2-\delta}$ carrier the appearance of $C^{18}O_2$ (Fig. 11c) is faster and occurred to a larger extent than in the case of Pt supported on $Ce_{0.2}La_{0.8}O_{2-\delta}$. In particular, the quantity of lattice ^{18}O that
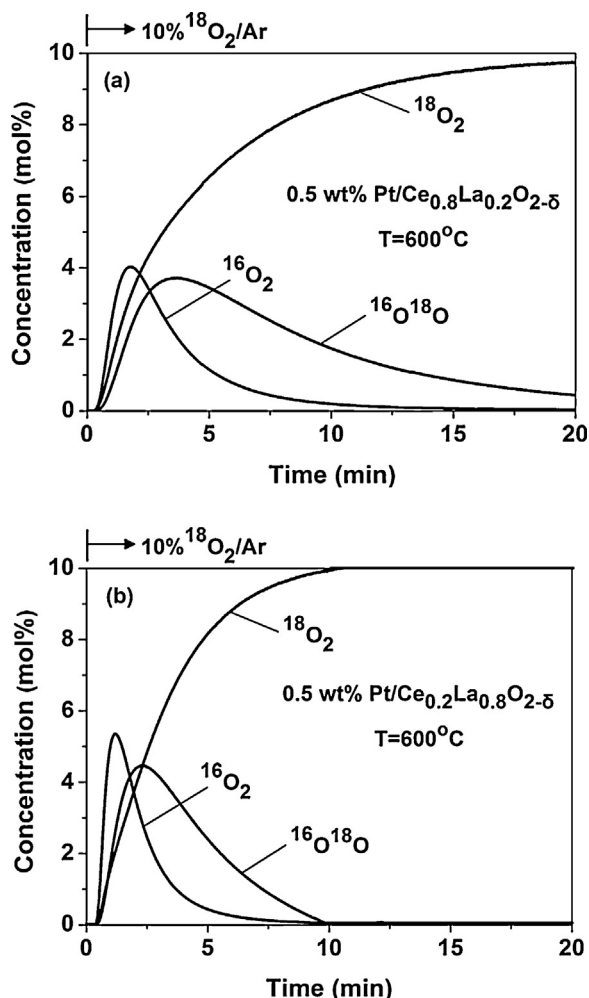
Fig. 12. Transient response curves of $^{16}O_2$, $^{16}O^{18}O$ and $^{18}O_2$ obtained during ^{18}O isotopic exchange performed at 600 °C on 0.5 wt% Pt/Ce$_{0.8}$La$_{0.2}$O$_{2-\delta}$ (a) and 0.5 wt% Pt/Ce$_{0.2}$La$_{0.8}$O$_{2-\delta}$ catalysts according to the gas switch: Ar → 10 vol% $^{18}O_2$/Ar (t).

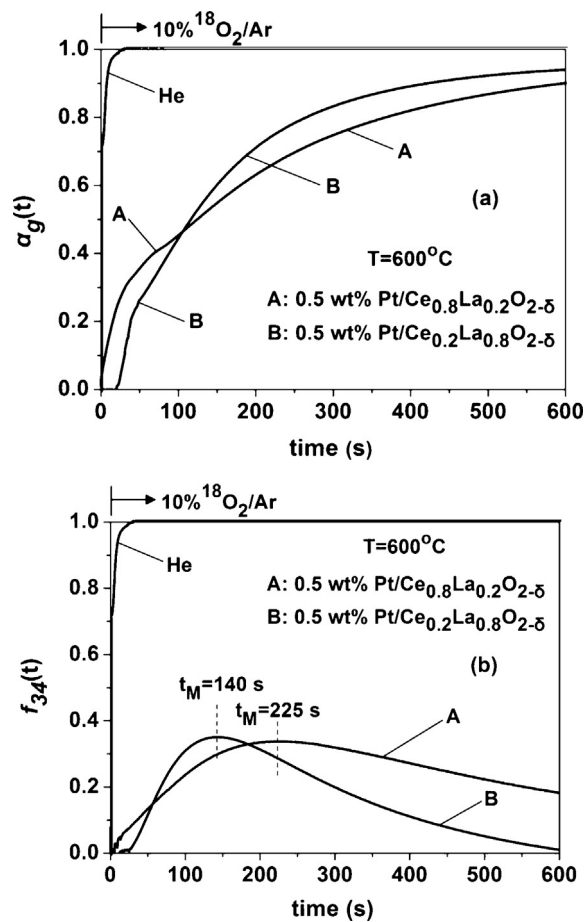**Fig. 13.** The estimated $\alpha_g(t)$ (a) and $f_{34}(t)$ (b) transient response curves obtained over 0.5 wt% Pt/Ce$_{0.8}$La$_{0.2}$O$_{2-\delta}$ and 0.5 wt% Pt/Ce$_{0.2}$La$_{0.8}$O$_{2-\delta}$ catalysts according to the gas switch: Ar → 10 vol% $^{18}O_2$/Ar (t) (see Fig. 12).

participated in the formation of both C$^{16}O^{18}O$ and C$^{18}O_2$ was 0.74 and 0.13 mmol/g, respectively for Pt/Ce$_{0.8}$La$_{0.2}$O$_{2-\delta}$ (Fig. 11a) and Pt/Ce$_{0.2}$La$_{0.8}$O$_{2-\delta}$ (Fig. 11b).

Fig. 12 presents transient response curves of all three di-oxygen isotopes obtained under the transient ^{18}O-isotopic exchange experiment conducted at 600 °C (Section 2.2.4). The amounts of exchangeable oxygen derived from the solid catalyst and appeared as $^{16}O_2$ and $^{16}O^{18}O$ in the gas phase were found to be 3.55 and 9.0 mmol/g, respectively for Pt/Ce$_{0.8}$La$_{0.2}$O$_2$ and 2.75 and 4.8 mmol/g, respectively for Pt/Ce$_{0.2}$La$_{0.8}$O$_2$ during the first 20 min of the transient (Fig. 12). After plotting the $\alpha_g(t)$ and $f_{34}(t)$ functions vs. time (Fig. 13), two important features of the transient ^{18}O-isotopic exchange are observed. The first one is the delay (~20 s) in the appearance of the transient response curves for the two solids, and the significantly lower values they take in the first 50 s after exposure of the solid in the $^{18}O_2$/Ar isotope gas. The second one are the differences observed in the shape and position of the $f_{34}(t)$ function between the two catalysts. The latter reflects differences in surface and bulk oxygen diffusion and surface oxygen exchange processes [30]. It is seen that the greater is the degree of La^{3+} substitution for Ce^{4+} (decrease of Ce/La atom ratio) in Ce$_{1-x}$La$_x$O$_{2-\delta}$ support the higher is the overall rate of surface oxygen exchange.

XRD data of the present Ce$_{1-x}$La$_x$O$_{2-\delta}$ solids reported elsewhere [35], and other XRD studies performed on Ce$_{1-x}$La$_x$O$_{2-\delta}$ [39,41] showed that by increasing the La/Ce ratio in the Ce$_{1-x}$La$_x$O$_{2-\delta}$

support composition the lattice constant, α (Å), increases, thus the O—O bond length increases, and therefore the O—O bond energy decreases. On the other hand, EXAFS studies [40] have indicated that the Ce—O bond length decreases by 0.06 Å when $x/1 - x$ varies in the 0.0–0.24 range, whereas the La—O bond length remains unaffected. Also, as previously mentioned, the solubility limit of La^{3+}-dopant in ceria is reached at $x \sim 0.52$ [41], thus, beyond this value the formation of La$_2$O$_{3-\delta}$ phase is expected. Based on (i) the above remarks, (ii) the transient isotopic C$^{18}O_2$ results presented in Fig. 11c, and (iii) the catalytic results of Fig. 2, it is suggested that the WGS reaction mechanism via the redox route is favored on Pt/Ce$_{1-x}$La$_x$O$_{2-\delta}$ the support of which contains less mobile surface oxygen species (e.g. Ce$_{0.8}$La$_{0.2}$O$_{2-\delta}$ vs. Ce$_{0.2}$La$_{0.8}$O$_{2-\delta}$).

4. Conclusions

Ce$_{1-x}$La$_x$O$_{2-\delta}$ prepared by the citrate sol–gel method at compositions in the $0.0 < x < 0.5$ range form solid solutions. At all compositions investigated ($x = 0.0, 0.2, 0.5, 0.8$ and 1.0), these metal oxide supports provide high dispersions for 0.5 wt% Pt loading ($D = 80$–100%) with the concomitant formation of very small Pt particles (1.0–1.4 nm) after calcination (20%O$_2$/He) at 600 °C for 2 h and reduction (H$_2$, 1 bar) at 300 °C for 2 h. Doping of CeO$_2$ at the level of 20 at.% La^{3+} (Ce/La = 4/1) largely increases the specific reaction rate per gram basis (μmol CO g^{-1} s^{-1}) and per length of perimeter of Pt-support interface (μmol CO cm^{-1} s^{-1}) of Pt/Ce$_{0.8}$La$_{0.2}$O$_{2-\delta}$ catalyst when compared to Pt/CeO$_2$. On the other hand, at the level of La^{3+}-content in the 50–80 at.% range, the specific activity drops.

This result is related to the positive effect of La^{3+}-doping of ceria at the level of 20 at.% on important surface and bulk physico-chemical properties of $Pt/Ce_{0.8}La_{0.2}O_{2-\delta}$ catalytic system. The latter have strong influence on the site reactivity at the Pt-support interface [23], according to the following observations:

(a) The oxygen storage capacity (OSC) of $Pt/Ce_{0.8}La_{0.2}O_{2-\delta}$ measured in the 250–550 °C range, and which is directly linked to the concentration of oxygen vacancies in the $Ce_{1-x}La_xO_{2-\delta}$ support, was found to be the largest among the series of catalysts investigated. On the other hand, on the basis of transient ^{18}O isotopic exchange studies, $Pt/Ce_{0.8}La_{0.2}O_{2-\delta}$ exhibits a lower overall rate of surface oxygen exchange than $Pt/Ce_{0.2}O_{0.8}O_{2-\delta}$, suggesting that the rate of WGS *via* the "redox" mechanism requires less mobile surface oxygen. Surface oxygen vacant sites inherently present in $Ce_{1-x}La_xO_{2-\delta}$ seem to be offered more readily toward water dissociation than bulk oxygen diffusion during WGS reaction conditions.
(b) The support of $Pt/Ce_{0.8}La_{0.2}O_{2-\delta}$ (Ce/La = 4/1) with the best catalytic activity and performance was found to present the lowest energy band gap among the other supports. This is likely linked to an optimum electron transfer between Pt and $Ce_{0.8}La_{0.2}O_{2-\delta}$ support, which influences to a positive manner the oxidation state of Pt, and likely the energetics of CO chemisorption. In fact, the surface concentration of two of the main types of linear adsorbed CO formed (DRIFTS studies), and the Pt^{2+}/Pt^{4+} ratio (UV–vis/DRS studies) are largely influenced by the Ce/La atom ratio in the support chemical composition.
(c) $Pt/Ce_{0.8}La_{0.2}O_{2-\delta}$ (Ce/La = 4/1) exhibits the best stable catalytic performance with TOS (up to 70 h) due largely to the low amount of accumulated "carbon" and carbonate-type adsorbed species. The amount of "carbon" was found to be influenced by the Ce/La atom ratio in the support chemical composition, as a result of its influence on the concentration of support's basic sites that promote "carbon" gasification.

Acknowledgements

References

[1] D.S. Newsome, Catalysis Reviews: Science and Engineering 21 (1980) 275–318.
[2] C. Ratnasamy, J.P. Wagner, Catalysis Reviews 51 (2009) 325–440.
[3] K. Polychronopoulou, C.M. Kalamaras, A.M. Efstathiou, Recent Patents on Materials Science 4 (2011) 122–145.
[4] X. Cheng, Z. Shi, N. Glass, L. Zhang, J. Zhang, D. Song, Z.-S. Liu, H. Wang, J. Shen, Journal of Power Sources 165 (2007) 739–756.
[5] A. Qi, B. Peppley, K. Karan, Fuel Processing Technology 88 (2007) 3–22.
[6] A.M. Duarte de Farias, A.P.M.G. Barandas, R.F. Perez, M.A. Fraga, Journal of Power Sources 165 (2007) 854–860.
[7] P. Panagiotopoulou, D.I. Kondarides, Catalysis Today 112 (2006) 49–52.
[8] P. Panagiotopoulou, J. Papavasiliou, G. Avgouropoulos, T. Ioannides, D.I. Kondarides, Journal of Chemical Engineering 134 (2007) 16–22.
[9] A.M. Duarte de Farias, D. Nguyen-Thanh, M.A. Fraga, Applied Catalysis B: Environmental 93 (2010) 250.
[10] D.-W. Jeong, H.S. Potdar, H.-S. Roh, Catalysis Letters 142 (2012) 439–444.
[11] Y.T. Kim, S.J. You, E.D. Park, International Journal of Hydrogen Energy 37 (2012) 1465–1474.
[12] L.Z. Linganiso, G. Jacobs, K.G. Azzam, U.M. Graham, B.H. Davis, D.C. Cronauer, A.J. Kropf, C.L. Marshall, Applied Catalysis A: General 394 (2011) 105–116.
[13] L.Z. Linganiso, V.R.R. Pendyala, G. Jacobs, B.H. Davis, D.C. Cronauer, A.J. Kropf, C.L. Marshall, Catalysis Letters 141 (2011) 1723–1731.
[14] C.M. Kalamaras, I.D. Gonzalez, R.M. Navarro, J.L.G. Fierro, A.M. Efstathiou, Journal of Physical Chemistry C 115 (2011) 11595–11610.
[15] Y. Wang, S. Liang, A. Cao, R.L. Thompson, G. Veser, Applied Catalysis B: Environmental 99 (2010) 89–95.
[16] J.M. Zalc, V. Sokolovskii, D.G. Loffler, Journal of Catalysis 206 (2002) 169–171.
[17] X. Liu, W. Ruettinger, X. Xu, R. Farrauto, Applied Catalysis B: Environmental 56 (2005) 69–75.
[18] T. Bunluesin, R.J. Gorte, G.W. Graham, Applied Catalysis B: Environmental 15 (1998) 107–114.
[19] X. Wang, R.J. Gorte, J.P. Wagner, Journal of Catalysis 212 (2002) 225–230.
[20] G. Jacobs, B.H. Davis, Catalysis 20 (2007) 122–285.
[21] C.M. Kalamaras, P. Panagiotopoulou, D.I. Kondarides, A.M. Efstathiou, Journal of Catalysis 264 (2009) 117–129.
[22] C.M. Kalamaras, S. Americanou, A.M. Efstathiou, Journal of Catalysis 279 (2011) 287–300.
[23] C.M. Kalamaras, K.C. Petallidou, A.M. Efstathiou, Applied Catalysis B: Environmental 136–137 (2013) 225–238.
[24] C.M. Kalamaras, D.D. Dionysiou, A.M. Efstathiou, ACS Catalysis 2 (2012) 2729–2742.
[25] C.N. Costa, T. Anastasiadou, A.M. Efstathiou, Journal of Catalysis 194 (2000) 250–265.
[26] H.C. Yao, Y.F.Y. Yao, Journal of Catalysis 86 (1984) 254–265.
[27] P.S. Lambrou, C.N. Costa, S.Y. Christou, A.M. Efstathiou, Applied Catalysis B: Environmental 54 (2004) 237–250.
[28] S.Y. Christou, A.M. Efstathiou, Topics in Catalysis 42-43 (2007) 351–355.
[29] P.S. Lambrou, K. Polychronopoulou, K.C. Petallidou, A.M. Efstathiou, Applied Catalysis B: Environmental 111 (2012) 349–359.
[30] D.V. Ivanov, E.M. Sadovskaya, L.G. Pinaeva, L.A. Isupova, Journal of Catalysis 267 (2009) 5–13.
[31] P. Kubelka, F. Munk, Z Tech Phys 12 (1931) 593–601.
[32] D.G. Barton, M. Shtein, R.D. Wilson, S.L. Soled, E. Iglesia, Journal of Physical Chemistry B 103 (1999) 630–640.
[33] G. Tsilomelekis, S. Boghosian, Journal of Physical Chemistry C 115 (2011) 2146–2154.
[34] K. Polychronopoulou, C.N. Costa, A.M. Efstathiou, Applied Catalysis A: General 272 (2004) 37–52.
[35] K.C. Petallidou, K., Polychronopoulou, A.M. Efstathiou, Conference Papers in Energy, Power Options for the Eastern Mediterranean Region, Hindawi Publishing Corporation (in press).
[36] M.-F. Luo, Z.-L. Yan, L.-Y. Jin, M. He, Journal of Physical Chemistry B 110 (2006) 13068–13071.
[37] M. Alifanti, B. Baps, N. Blangenois, J. Naud, P. Grange, B. Delmon, Chemistry of Materials 15 (2003) 395–403.
[38] R.O. Fuentes, R.T. Baker, Journal of Physical Chemistry C 113 (2009) 914–924.
[39] F. Deganello, A. Martorana, Journal of Solid State Chemistry 163 (2002) 527–533.
[40] F. Deganello, A. Longo, A. Martorana, Journal of Solid State Chemistry 175 (2003) 289–298.
[41] B.C. Morris, W.R. Flavell, W.C. Mackrodt, M.A. Morris, Journal of Materials Chemistry 3 (1993) 1007–1013.
[42] J.W. Niemantsverdriet, Spectroscopy in Catalysis: An Introduction, 3rd ed., Wiley, New York, 2007.
[43] B.M. Reddy, L. Katta, G. Thrimurthulu, Chemistry of Materials 22 (2010) 467–475.
[44] K. Krishna, A. Bueno-Lopez, M. Makkee, J.A. Moulijn, Applied Catalysis B: Environmental 75 (2007) 210–220.
[45] L. Garcia, R. French, S. Czernik, E. Chornet, Applied Catalysis A: General 201 (2000) 225–239.
[46] T. Borowiecki, A. Mochocki, J. Ryczkowski, in: C.H. Bartholomew, J.B. Butt (Eds.), Catalyst Deactivation, Elsevier, Amsterdam, 1994, p. 537.
[47] T. Borowiecki, Applied Catalysis 10 (1984) 273–289.
[48] R.W. McCabe, L.D. Schmidt, Surface Science 60 (1976) 85–98.
[49] T. Arakawa, K. Takada, Y. Tsunemine, J. Shiokawa, Materials Research Bulletin 24 (1989) 395–402.
[50] F. Huber, Z. Yu, J.C. Walmsley, D. Chen, H.J. Venvik, A. Holmen, Applied Catalysis B: Environmental 71 (2007) 7–15.
[51] T. Ioannides, X.E. Verykios, Journal of Catalysis 140 (1993) 353–369.
[52] J.S. Rieck, A.T. Bell, Journal of Catalysis 96 (1985) 88–105.
[53] R. Barth, R. Pitchai, R.L. Anderson, X.E. Verykios, Journal of Catalysis 116 (1989) 61–70.
[54] J. Rasko, Journal of Catalysis 217 (2003) 478–486.
[55] P. Panagiotopoulou, D.I. Kondarides, Applied Catalysis B: Environmental 101 (2011) 738–746.
[56] G.S. Lane, E.E. Wolf, Journal of Catalysis 105 (1987) 386–404.
[57] P. Panagiotopoulou, D.I. Kondarides, Journal of Catalysis 260 (2008) 141–149.
[58] M. Primet, J.M. Basset, M.V. Mathieu, M. Prettre, Journal of Catalysis 29 (1973) 213–223.
[59] M. Primet, Journal of Catalysis 88 (1984) 273–282.
[60] A. Yee, S.J. Morrison, H. Idriss, Journal of Catalysis 191 (2000) 30–45.
[61] A. Bensalem, J.C. Muller, F. Bozon-Verduraz, Journal of the Chemical Society, Faraday Transactions 88 (1992) 153–154.
[62] A. Bensalem, F. Bozon-Verduraz, M. Delamar, G. Bugli, Applied Catalysis A: General 121 (1995) 81–93.
[63] J. Choi, H. Park, M.R. Hoffman, Journal of Materials Research 25 (2010) 149–158.
[64] J. Zhensheng, X. Chanjuan, Z. Qingmei, Y. Feng, Z. Jiazheng, X. Jinzhen, Journal of Molecular Catalysis A: Chemical 191 (2003) 61–66.

[65] A.C.M. van den Broek, J. van Grondelle, R.A. Santen, Journal of Catalysis 167 (1997) 417–424.
[66] V.B. Mortola, S. Damyanova, D. Zanchet, J.M.C. Bueno, Applied Catalysis B: Environmental 107 (2011) 221–236.
[67] B.G. Mishra, G.R. Rao, Journal of Molecular Catalysis A: Chemical 243 (2006) 204–213.
[68] C. Binet, A. Badri, J.-C. Lavalley, Journal of Physical Chemistry 98 (1994) 6392–6398.
[69] Y. Yang, F. Su, S. Zhang, W. Guo, X. Yuan, Y. Guo, Colloids and Surfaces A: Physicochemical and Engineering Aspects 415 (2012) 399–405.
[70] L. Truffault, M.-T. Ta, T. Devers, K. Konstantivov, V. Harel, C. Simmonard, C. Andreazza, I.P. Nevirkovets, A. Pineau, O. Veron, J.-P. Blondeau, Materials Research Bulletin 45 (2010) 527–535.
[71] R.S. Weber, Journal of Catalysis 151 (1995) 470–474.
[72] X.-S. Huang, H. Sun, L.-C. Wang, Y.-M. Liu, K.-N. Fan, Y. Cao, Applied Catalysis B: Environmental 90 (2009) 224–232.
[73] G.R. Bamwenda, H. Arakawa, Journal of Molecular Catalysis A: Chemical 161 (2000) 105–113.
[74] C.A. Hogath, Z.T. Al-Dhhan, Physical Status Solidi B 137 (1986) K157.
[75] K.B. Sundaram, P. Wahid, Physical Status Solidi B 161 (1990) K64.
[76] M.H. Chowdhury, M.A. Mannan, S.A. Mahmood, International Journal of Emerging Technologies in Sciences and Engineering 2 (2010) 1–12.
[77] S. Tsunakawa, J.-T. Wang, Y. Kawazoe, Journal of Alloys and Compounds 408-412 (2006) 1145–1148.
[78] B.-S. Huang, F.-Y. Chang, M.-Y. Wey, International Journal of Hydrogen Energy 35 (2010) 7699–7705.
[79] V.G. Keramidas, W.B. White, Journal of Chemical Physics 59 (1973) 1561–1562.
[80] G. Gouadec, P. Colomban, Progress in Crystal Growth and Characterization of Materials 53 (2007) 1–56.
[81] W.Y. Hernandez, O.H. Laguna, M.A. Centeno, J.A. Odriozola, Journal of Solid State Chemistry 184 (2011) 3014–3020.
[82] Z.D. Dohcevic-Mitrovic, M. Radovic, M. Scepanovic, M. Grujic-Brojcin, Z.V. Popovic, B. Matovic, S. Boskovic, Applied Physics Letters 91 (2007) 203118–203123.
[83] J.R. McBride, K.C. Hass, B.D. Poindexter, W.H. Weber, Journal of Applied Physics 76 (1994) 2435–2441.
[84] A. Bueno-Lopez, K. Krishna, M. Makkee, J.A. Moulijn, Journal of Catalysis 230 (2005) 237–248.
[85] E. Yu Pikalova, A.A. Murashkina, V.I. Maragou, A.K. Demin, V.N. Strekalovsky, P.E. Tsiakaras, International Journal of Hydrogen Energy 36 (2011) 6175–6183.
[86] L. Katta, P. Sudarsanam, G. Thrimurthulu, B.M. Reddy, Applied Catalysis B: Environmental 101 (2010) 101–108.
[87] P. Panagiotopoulou, A. Christodoulakis, D.I. Kondarides, S. Boghosian, Journal of Catalysis 240 (2006) 114–125.